Monthly Notices
of the
ROYAL ASTRONOMICAL SOCIETY

MNRAS **465,** 722–738 (2017)
Advance Access publication 2016 October 26

doi:10.1093/mnras/stw2740

Size evolution of normal and compact galaxies in the EAGLE simulation

M. Furlong,[1⋆] R. G. Bower,[1⋆] R. A. Crain,[2] J. Schaye,[3] T. Theuns,[1] J. W. Trayford,[1] Y. Qu,[1] M. Schaller,[1] M. Berthet[1] and J. C. Helly[1]

[1]*Institute for Computational Cosmology, Durham University, South Road, Durham DH1 3LE, UK*
[2]*Astrophysics Research Institute, Liverpool John Moores University, 146 Brownlow Hill, Liverpool L3 5RF, UK*
[3]*Leiden Observatory, Leiden University, PO Box 9513, NL-2300 RA Leiden, the Netherlands*

Accepted 2016 October 21. Received 2016 October 20; in original form 2015 October 19

ABSTRACT

We present the evolution of galaxy sizes, from redshift 2 to 0, for actively star forming and passive galaxies in the cosmological hydrodynamical 100^3 cMpc^3 simulation of the EAGLE project. We find that the sizes increase with stellar mass, but that the relation weakens with increasing redshift. Separating galaxies by their star formation activity, we find that passive galaxies are typically smaller than active galaxies at a fixed stellar mass. These trends are consistent with those found in observations and the level of agreement between the predicted and observed size–mass relations is of the order of 0.1 dex for $z < 1$ and 0.2–0.3 dex from redshift 1 to 2. We use the simulation to compare the evolution of individual galaxies with that of the population as a whole. While the evolution of the size–stellar mass relation for active galaxies provides a good proxy for the evolution of individual galaxies, the evolution of individual passive galaxies is not well represented by the observed size–mass relation due to the evolving number density of passive galaxies. Observations of $z \sim 2$ galaxies have revealed an abundance of massive red compact galaxies, which depletes below $z \sim 1$. We find that a similar population forms naturally in the simulation. Comparing these galaxies with their $z = 0$ descendants, we find that all compact galaxies grow in size due to the high-redshift stars migrating outwards. Approximately 60 per cent of the compact galaxies increase in size further due to renewed star formation and/or mergers.

Key words: galaxies: evolution – galaxies: high-redshift – galaxies: star formation – galaxies: structure.

1 INTRODUCTION

Understanding and reproducing the observed evolution of galaxies is one of the key aims of modern cosmology. Galaxies are thought to form as a result of gas cooling in the gravitational potential dominated by dark matter (e.g. White & Rees 1978; White & Frenk 1991). As the baryons cool, they form a rotating disc. Assuming that the gas initially has a specific angular momentum similar to that of the dark matter and that the angular momentum is conserved, the Λ cold dark matter (ΛCDM) framework predicts the evolution of the sizes of disc galaxies (Fall & Efstathiou 1980; Mo, Mao & White 1998). In practice, however, the process of baryon condensation is complicated by the formation of stars and black holes, and the energy which they feed back into the surrounding gas. The angular momentum of the stars which form may therefore differ significantly from that of the halo. The evolution of galaxy sizes is therefore a critical test of the physical processes of galaxy formation.

Recent observational surveys of the $z \sim 0$ Universe sample millions of galaxies, probing the full range of galaxy masses and sizes (e.g. Shen et al. 2003; Dutton et al. 2011; Baldry et al. 2012). The evolution of the sizes of galaxies from the present day up to redshift 3 has been mapped for a broad range of galaxy masses and types using the *Hubble Space Telescope* with CANDELS imaging (Bezanson et al. 2009; Patel et al. 2013; van Dokkum et al. 2014; van der Wel et al. 2014, hereafter VDW14). Galaxies in the distant Universe are smaller at a fixed mass than local systems, suggesting that galaxies undergo significant size evolution.

At $z \gtrsim 1$, observations reveal a class of very compact passive galaxies, often referred to as 'red nuggets' (e.g. Cimatti et al. 2004; Daddi et al. 2005; Trujillo et al. 2006). Such galaxies are rare in the nearby Universe (Poggianti et al. 2013b; VDW14). The evolutionary path of individual compact galaxies cannot be inferred from the observational data alone since galaxies evolve in both stellar mass and size, and may merge with other systems. Mergers with other galaxies, in particular, may result in significant size growth even if relatively little mass is added to the system (e.g. Naab, Johansson & Ostriker 2009; Hopkins et al. 2010; Oser et al. 2012; Hilz, Naab &

⋆ E-mail: mfurlong@tcd.ie (MF); r.g.bower@durham.ac.uk (RGB)

Ostriker 2013). It is thus challenging to establish what becomes of these compact passive galaxies from observational evidence alone (e.g. van Dokkum et al. 2015). Simulations, such as the one considered here, can provide the necessary link to the present-day galaxy population.

Until recently, the sizes of galaxies produced by hydrodynamical simulations were not consistent with observations: While the masses of the galaxies tended to be too large, their sizes were too small (e.g. Scannapieco et al. 2012). The dense gas transfers angular momentum to the outer halo, which is exacerbated if too much gas is turned into stars, leading to what became known as the angular momentum catastrophe (Katz & Gunn 1991; Navarro & White 1994). This problem can be overcome by the inclusion of energetic feedback, which tends to expel the lowest angular momentum gas from the forming galaxy, while also regulating the stellar mass formed (e.g. Sales et al. 2010; Brook et al. 2011, 2012a). Including realistic and efficient feedback has resulted in more reasonable galaxy sizes for disc galaxies in small galaxy samples or over specific mass ranges (Governato et al. 2004; Okamoto & Millis 2005; Sales et al. 2010; Brook et al. 2012b; McCarthy et al. 2012; Aumer et al. 2013; Munshi et al. 2013; Hopkins et al. 2014; Marinacci, Pakmor & Springel 2014). However, reproducing the observed sizes of the general galaxy population remains a challenge for many cosmological simulations. The production of realistic galaxy stellar masses in such simulations, or indeed a broad range of galaxy scaling relations, is a necessary, but not sufficient, criterion for the reproduction of galaxy sizes (Scannapieco et al. 2012; Crain et al. 2015).

The distribution of galaxy sizes has been studied in cosmological simulations in the work of Sales et al. (2010) and McCarthy et al. (2012), who focused on the $z = 2$ and 0 populations in the OWLS (Schaye et al. 2010) and GIMIC (Crain et al. 2009) simulations, respectively. A recent study based on the ILLUSTRIS simulation (Vogelsberger et al. 2014) by Snyder et al. (2016) examined the size–mass–morphology relation at $z = 0$. The galaxy sizes were shown to be a factor of $\sim$2 too large relative to observations at this redshift, and the evolution of sizes was not examined. Using the same simulation, Wellons et al. (2015a,b) looked at the formation and evolution of $z = 2$ massive compact galaxies, respectively. The size evolution of the compact galaxies was found to depend on the environment in which the galaxies are found. We will also examine the evolution of compact galaxies, but in the broader context of the high-z passive population in the simulation, after comparing the full galaxy population with observations, finding a good agreement.

In this study, we investigate the evolution of the galaxy size–mass relation and evolutionary tracks of individual galaxies using the Evolution and Assembly of Galaxies and their Environments (EAGLE) simulation suite (Schaye et al. 2015; Crain et al. 2015). The largest of the EAGLE simulations evolves a volume of 100^3 comoving Mpc^3 (cMpc^3), with 13 200 galaxies of stellar mass $M_* > 10^9$ M$_\odot$ and 3562 galaxies with $M_* > 10^{10}$ M$_\odot$ at $z = 0$. This sample enables us to study the evolution of galaxy sizes from $z = 2$ to the present day, while separating the population into those that are star forming and those that are passive.

The simulation combines gravitational N-body solvers with state-of-the-art smoothed particle hydrodynamics and subgrid models for the formation of stars, metal-dependent cooling, stellar mass-loss, and energy injection from stars and black holes. The simulation reproduces a wide range of properties of observed galaxies with unprecedented fidelity (Schaye et al. 2015). The observed *present-day* galaxy stellar mass function, galaxy disc sizes and black hole masses were used to calibrate the uncertain parameters of the subgrid components, but other aspects of the model, such as the star formation rates (SFRs; Schaye et al. 2015), galaxy colours (Trayford et al. 2015), rotation curves (Schaller et al. 2015b), the gas content of galaxies (Lagos et al. 2015; Bahé et al. 2016), and the intergalactic hydrogen and metal absorption lines (Schaye et al. 2015; Rahmati et al. 2015), as well as the evolution of the galaxy stellar mass function and SFRs (Furlong et al. 2015), represent predictions of the simulation and exhibit a broad agreement with observations. A full discussion of the model calibration/validation philosophy can be found in Schaye et al. (2015) and Crain et al. (2015).

Although the $z = 0$ galaxy disc sizes were considered during the calibration of the EAGLE simulation, the *evolution* of galaxy sizes is a prediction of the simulation. Moreover, the simulations allow us to explore the difference in size between galaxies which are actively forming stars and those that are passive, a distinction that was not made during the calibration. Passive galaxies are particularly prevalent at high stellar masses, and primarily grow in mass through galaxy mergers. Such galaxies are observed to be smaller than disc galaxies of the same stellar mass (e.g. Shen et al. 2003; Baldry et al. 2012; VDW14), providing a key test of the simulation. This comparison has further implications than simply validating the model since the simulation can also help us interpret the observational data. For example, we can trace galaxies as they evolve, enabling us to address issues such as the origin of the size–mass relation and to relate galaxy masses and sizes at one redshift to another redshift. In particular, we will show that the simulation produces a population of high-redshift compact galaxies, and we trace the descendants of these galaxies to examine their properties at the present day.

The layout of this paper is as follows. Brief descriptions of the EAGLE simulations and the galaxy selection can be found in Section 2, where we also discuss the sensitivity of galaxy size to its definition. In Section 3, we consider the sizes of the full galaxy population. We compare the sizes of simulated galaxies, and their evolution, with observational measurements in Section 3.1, finding a good agreement, particularly relative to previous simulation results (Appendix A). In Section 3.2, we determine the origin of the scatter in the size–mass relation. We then explore the evolution of individual galaxies in Section 3.3 and the mass dependence of the size growth in Section 3.4. In Section 4, we look at the evolution of high-redshift passive galaxies, with a particular focus on compact galaxies. A summary of our main findings and concluding remarks are presented in Section 5.

2 GALAXIES IN THE EAGLE SIMULATIONS

The production and selection of simulated galaxies are described below. We begin with an overview of the primary EAGLE simulation in Section 2.1, followed by a discussion of the definition and selection of galaxies applied to the simulation in Section 2.2. In Section 2.3, we present our definition of galaxy size and discuss alternative choices. Further details on alternative galaxy size definitions can be found in Appendix C. Finally, the galaxy classification applied in this study is introduced and discussed in Section 2.4, with further details given in Appendix D.

2.1 Simulation overview

For this study, we use cosmological hydrodynamical simulations from the EAGLE project. We focus primarily on the largest of the simulations, Ref-L100N1504, a $(100\ \mathrm{cMpc})^3$ simulation with baryonic particle masses of 1.2×10^6 M$_\odot$, which provides a large sample of galaxies resolved by at least 1000 star particles. These

Table 1. Simulation box size, particle number, initial baryonic and dark matter particle masses, and maximum gravitational force softening for Ref-L100N1504, Recal-L025N0752 and Ref-L025N0752 simulations.

Simulation	Box size (cMpc)	$N_{\rm part}$	$m_{\rm g}$ ($\rm M_\odot$)	$m_{\rm dm}$ ($\rm M_\odot$)	ϵ^a (pkpc)
L100N1504	100	2×1504^3	1.81×10^6	9.70×10^6	0.70
L025N0752	25	2×752^3	2.26×10^5	1.21×10^6	0.35

Note. [a]For the redshift range covered in this paper, the gravitational softening is fixed in the listed physical coordinates. At redshifts above 2.8, it is fixed in comoving coordinates.

galaxies span more than two orders of magnitude in stellar mass and are found in a diverse range of environments.

We also analyse two smaller, higher resolution simulations, Recal-L025N0752 and Ref-L025N0752. The high-resolution simulations are used for convergence tests presented in Appendix B. The box sizes and resolutions of these simulations are summarized in Table 1. The Ref-L025N0752 simulation has a factor of 8 (2) better mass (spatial) resolution and employs the same subgrid parameters as Ref-L100N1504; comparing these two simulations tests the strong convergence of the simulation [see Schaye et al. (2015) for definitions and discussion of the concepts of 'strong' and 'weak' convergence]. Recal-L025N0752 also has a factor of 8 better mass resolution but was recalibrated to better reproduce the observed local Universe galaxy stellar mass function at this higher resolution. This simulation enables examination of the weak convergence of the simulation.

The EAGLE simulation suite adopts a flat ΛCDM cosmogony with parameters inferred from the *Planck* data (Planck Collaboration XVI 2014); $\Omega_\Lambda = 0.693$, $\Omega_{\rm m} = 0.307$, $\Omega_{\rm b} = 0.048$, $\sigma_8 = 0.8288$, $n_{\rm s} = 0.9611$ and $H_0 = 67.77\,{\rm km\,s^{-1}}$ Mpc^{-1}. The Chabrier (2003) stellar initial mass function (IMF) is adopted. Galaxy stellar masses are computed by summing the mass of star particles located within a spherical aperture of 30 physical kiloparsecs (pkpc) centred on the potential minimum of the galaxy, as used by Schaye et al. (2015). SFRs are computed within the same aperture. Galaxy sizes are quoted in physical units (e.g. pkpc), unless stated otherwise.

A complete description of the EAGLE code and subgrid physics was presented by Schaye et al. (2015); here, we provide a concise overview. Initial conditions at $z = 127$ were generated using second-order Lagrangian perturbation theory (Jenkins 2010). The initial conditions were evolved using a parallel *N*-body smooth particle hydrodynamics (SPH) code, a modified version of GADGET-3 (based on GADGET-2, last described by Springel 2005). The SPH implementation in EAGLE includes the Hopkins (2013) pressure-entropy formulation, a time-step limiter (Durier & Dalla Vecchia 2012), artificial viscosity and conduction (Dehnen & Aly 2012), and the Wendland (1995) C2 kernel; this set of changes to the SPH is collectively referred to as ANARCHY (see appendix A of Schaye et al. 2015). ANARCHY alleviates the problems associated with standard SPH in modelling contact discontinuities and fluid instabilities. Schaller et al. (2015a) show, however, that at the resolution of EAGLE, the impact of the hydrodynamics solver on galaxy properties in simulations is small for $M_* \lesssim 10^{10.5}\,{\rm M_\odot}$.

To model astrophysical processes which occur on scales below the resolution of the simulation, subgrid schemes are applied. Included are subgrid models for radiative cooling and photoheating, star formation, stellar mass-loss and metal enrichment, stellar feedback from massive stars, black hole growth and feedback from active galactic nuclei (AGNs).

The cooling and photoheating model uses the implementation of Wiersma, Schaye & Smith (2009a). Abundances of 11 elements are considered when computing radiative cooling rates, tabulated from CLOUDY (version 07.02; Ferland et al. 1998) assuming ionization equilibrium and exposure to the cosmic microwave background, and the Haardt & Madau (2001) model for the evolving ultraviolet/X-ray background.

Above a metallicity-dependent density threshold, star particles form stochastically, with the SFR determined from the gas pressure such that it reproduces the observed Kennicutt–Schmidt law (Kennicutt 1998; Schaye & Dalla Vecchia 2008). Star particles represent simple stellar populations described by a Chabrier IMF. The Jeans length for the cold phase of the interstellar medium (ISM) cannot be resolved by the simulations, and consequently, a pressure floor is imposed, corresponding to a polytropic equation of state ($P_{\rm eos} \propto \rho^{\gamma_{\rm eos}}$), enabling the multiphase ISM to be treated as a single-phase fluid.

Stellar mass-loss is based on the implementation of Wiersma et al. (2009b), where the mass lost from asymptotic giant branch stars, through winds of massive stars, and supernovae (both core collapse and Type Ia), is returned to the ISM over the lifetime of the stellar population.

Prompt feedback associated with star formation is implemented following Dalla Vecchia & Schaye (2012), where the thermal energy available from stars formed is stochastically distributed to neighbouring gas particles, without any preferential direction. Energy injection always results in a temperature increase of $\Delta T = 10^{7.5}$ K; such a temperature jump is required to mitigate numerical radiative losses at the resolution of the EAGLE simulations (Dalla Vecchia & Schaye 2012). We assume that a fraction $f_{\rm th}$ of the energy generated by the supernovae ($1.7 \times 10^{49}\,{\rm erg\,M_\odot^{-1}}$ for a Chabrier IMF) is distributed to neighbouring particles in this heating process. Note that $f_{\rm th}$ will be larger than unity if additional sources of energy, such as stellar winds, also contribute. A simple assumption is that $f_{\rm th}$ is a constant, but numerical considerations show that in dense gas the injected energy will be radiated before it can have a hydrodynamic effect (Dalla Vecchia & Schaye 2012). This problem will also be more evident in high-metallicity gas. We therefore parametrize $f_{\rm th}$ as

$$f_{\rm th} = f_{\rm th,min} + \frac{f_{\rm th,max} - f_{\rm th,min}}{1 + \left(\frac{Z}{0.1\,Z_\odot}\right)^{n_Z} \left(\frac{n_{\rm H,birth}}{n_{\rm H,0}}\right)^{-n_n}}, \quad (1)$$

where $n_{\rm H,\,birth}$ is the density inherited by the star particle, i.e. the density of its parent gas particle at the time it was converted into a stellar particle, and $n_{\rm H,\,0} = 0.67\,{\rm cm^{-3}}$ was chosen after comparing a few test simulations to the observed present-day Galaxy Stellar Mass Function (GSMF) and galaxy sizes. We found that the exact values of $f_{\rm th,\,max}$ and $f_{\rm th,\,min}$ had relatively little impact, and left them fixed at 3 and 0.3, respectively. For these limits, the mean and median energy injected over the course of the simulation are close to unity (1.06 and 0.7, respectively). Similarly, we fixed $n_Z = n_n = 2/\ln 10$ during early code development and left these values fixed.

In Crain et al. (2015), we show that the simplest model, $f_{\rm th} = 1$, results in a remarkably good fit to the observed present-day galaxy stellar mass function. It did not, however, provide a good description of galaxy sizes, with disc galaxies with mass around $10^{10.5}\,{\rm M_\odot}$ being a factor of 4 too small in size. Scaling $f_{\rm th}$ following equation (1), we obtain a good description of both the present-day GSMF and of galaxy sizes. The improvement is driven by the inclusion of a density dependence so that feedback is more efficient in high-density regions, compensating for the numerical losses. Increasing

the overall normalization of $f_{\rm th}$, or reducing $n_{\rm H,0}$, tends to increase galaxy sizes at a given stellar mass. This is due, at least in part, to the effect on the stellar mass–halo mass relation. See Schaye et al. (2015) and Crain et al. (2015) for further discussion on the motivation for this form of energy scaling.

The gas particle at the minimum of the potential of a halo is converted into a seed black hole of $10^5\ h^{-1}\ {\rm M}_\odot$ when a halo first reaches a mass of $10^{10}\ h^{-1}\ {\rm M}_\odot$ (Springel, Di Matteo & Hernquist 2005). The subgrid black hole accretes matter based on the modified Bondi–Hoyle model of Rosas-Guevara et al. (2016), adapted as described by Schaye et al. (2015), which reduces the accretion rate for high angular momentum gas. Of the matter accreted, a fraction of 0.015 of the rest-mass energy is returned to the surrounding medium in the form of energy. This feedback from AGNs is implemented thermally, as for the stellar feedback, but with a temperature jump of $\Delta T = 10^{8.5}$ K for Ref models and $\Delta T = 10^9$ K for the Recal model.

2.2 Sample selection

Galaxy identification is carried out as described by Schaye et al. (2015). The friends-of-friends method with a linking length of 0.2 identifies overdensities which we refer to as haloes. Self-bound substructures within haloes are identified using SUBFIND (Springel et al. 2001; Dolag et al. 2009). We refer to the stellar component of the subhaloes as the galaxies in the simulation. A central galaxy corresponds to the most massive subhalo within a halo.

To enable comparison to the observational study of VDW14, we bin galaxies in redshift intervals of $\Delta z = 0.5$. In the four redshift bins spanning $0 \leq z \leq 2$, we combine between three and six simulation outputs. We include galaxies with stellar masses $M_* > 10^9$ ${\rm M}_\odot$, to ensure that the masses, sizes and SFRs of galaxies are well sampled (see Schaye et al. (2015); Furlong et al. 2015, for convergence studies). We limit the sample to galaxies with $z \leq 2$ in order to minimize the dependence of the analysis on the very small ($R_{50} < 1$ pkpc) galaxies which are formed at higher redshifts.

An important question is to estimate the resolution of the simulation, and thus to decide on the smallest galaxies which can be reliably used in our analysis of galaxy growth. One way of defining the resolution of the simulation is to assume that the formation of star-forming gas is driven by gravity, and to use the gravitational softening. This would suggest a resolution of 0.7 pkpc. Gravity may not, however, be the limiting factor since dense gas is still able to fragment into small clumps due to pressure forces and efficient cooling. The simulation code uses a polytropic equation of state to regulate the masses of these clumps, but this does not translate into a resolution length scale. Indeed, in Appendix B, we present an analysis of the convergence of the simulation. The appendix shows that despite a factor of 8 decrease in particle mass, and a factor 2 decrease in softening length, the sizes of galaxies are hardly changed. The differences which do emerge can be explained as the result of differences in star formation histories. It appears therefore that galaxies larger than the softening scale can be used reliably. We therefore adopt the gravitational softening scale as an estimate for the resolution limit of the simulation, and show this as a horizontal line in all plots.

The sample contains 208 953 galaxies over the redshift range 0–2, of which 182 481 are actively forming stars and 26 472 are passive, as defined in Section 2.4. Further details of the galaxy sample can be found in Table 2.

We use galaxy merger trees to trace the evolution of individual galaxies. The merger trees are built by tracing the most bound particles of each subhalo between consecutive snapshots to determine the progenitor galaxies of all $z = 0$ galaxies. The main progenitor branch is that with the largest branch mass, as defined by De Lucia & Blaizot (2007). This method is similar to that of the D-halo merger trees described by Jiang et al. (2014). A full description of the trees is presented by Qu et al. (2017), with their public release[1] discussed by McAlpine et al. (2016).

Table 2. The number of galaxies with $M_* > 10^9$ ${\rm M}_\odot$ in different redshift bins between $z_{\rm low}$ and $z_{\rm high}$, including the division into active and passive galaxies based on SSFRs. The SSFR separating active and passive galaxies varies with redshift and is given by $\log_{10}({\rm SSFR}_{\rm lim}(z)/{\rm Gyr}^{-1}) = 0.5z - 2$, $z \in [0, 2]$.

$z_{\rm low}$	$z_{\rm high}$	Total	Active fraction	Passive fraction
0.0	0.5	80 816	0.78	0.22
0.5	1.0	65 682	0.90	0.10
1.0	1.5	34 669	0.95	0.05
1.5	2.0	27 786	0.97	0.03
0.0	2.0	208 953	0.87	0.13

2.3 Galaxy sizes

While the abundance, range and quality of the observational data available to measure galaxy sizes are continuously improving, the recovered sizes from the data typically depend, among other things, on the wavelength of the observations (Kelvin et al. 2012; VDW14; Lange et al. 2015), the assumed fitting profile (e.g. Head, Lucey & Hudson 2015) and the surface brightness of galaxies. While it is possible to 'observe' simulated galaxies in a similar way to real galaxies (Torrey et al. 2015; Trayford et al. 2016) and use these observations to measure galaxy sizes which can be compared with a particular data set, in this study, we are interested in the physical growth and evolution of galaxies, and in making predictions which can be compared with a variety of data sets. Hence, we use the physical half-stellar mass radius, R_{50}, as our definition of galaxy size, thus limiting systematic effects related to observations.

The half-mass radius is based on the total mass of all gravitationally bound stellar particles within a spherical aperture of radius 100 pkpc about the minimum of the gravitational potential of a galaxy. This definition of the half-mass radius of simulated galaxies is not directly dependent on the galaxy's shape or surface brightness. We apply the 100-pkpc aperture to ensure that star particles located far out in the halo, but which are assigned to the galaxy by the subhalo finder, are excluded from the calculation. The aperture affects only the most massive galaxies in the simulation, with $M_* > 10^{11}$ ${\rm M}_\odot$, as shown in Appendix C.

Note that the size definition here differs from that used by Schaye et al. (2015), where Sérsic fits to the projected stellar mass profile within 30-pkpc apertures were used to measure the half-mass radius. As mentioned above, in this study, we aim to avoid assumptions about the profile of the galaxies. A comparison between the sizes used by Schaye et al. (2015) and here can also be found in Appendix C.

[1] www.eaglesim.org/database.html

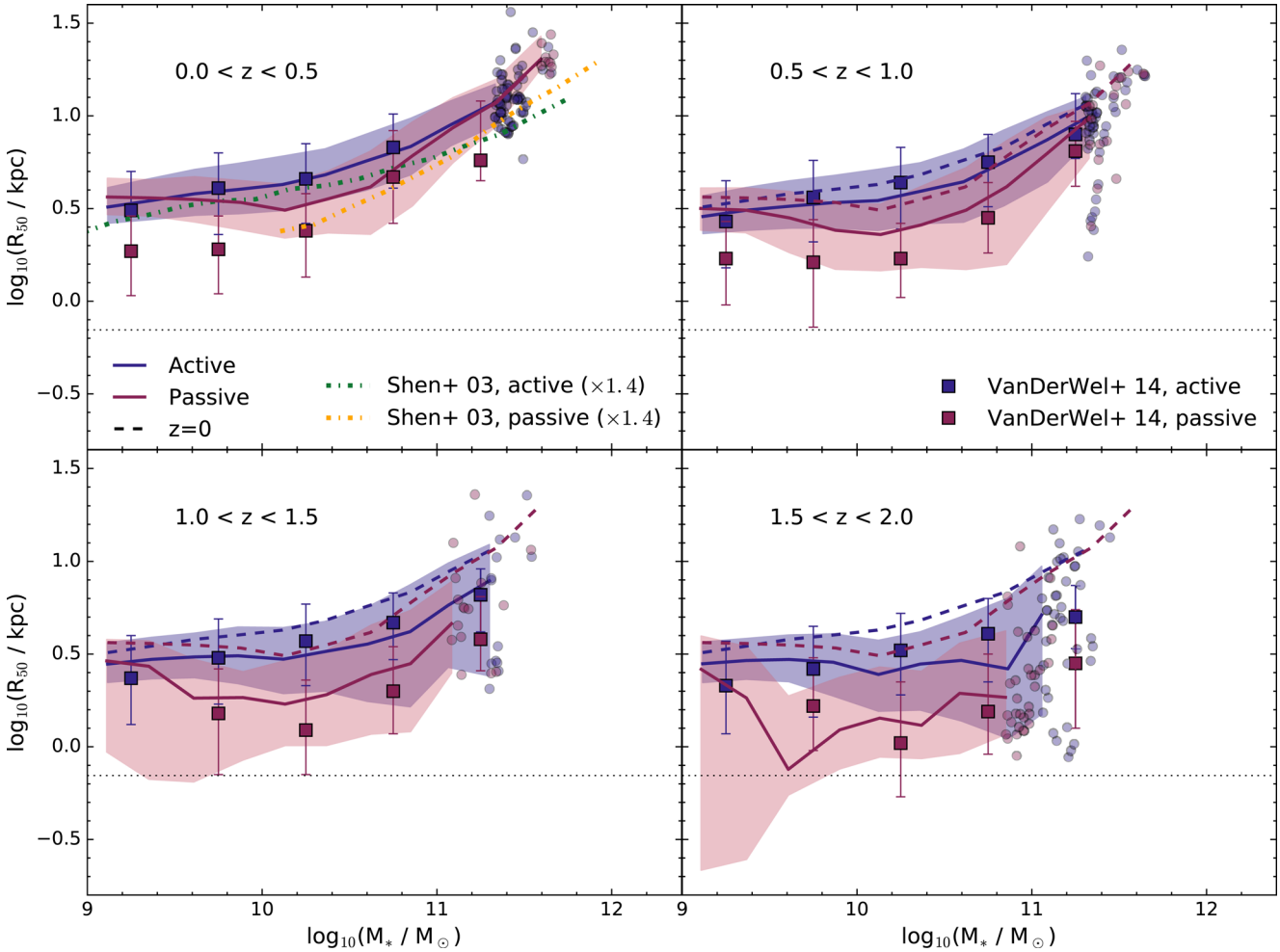

Figure 1. Galaxy size–mass relation in the Ref-L100N1504 EAGLE simulation compared with observations. Panels show different redshifts, from 0 to 2. Active and passive galaxies are shown in blue and red, respectively. The median relations from the simulation are shown by solid curves, whereas the shaded regions enclose the 16th to 84th percentiles. Bins of 0.2 dex in stellar mass are used. Individual points are shown for bins containing fewer than 10 galaxies. For reference, the dashed curves repeat the size–mass relation for active and passive galaxies from the lowest redshift bin. The horizontal dotted line corresponds to the gravitational force softening in the simulation, which is fixed at 0.7 pkpc over this redshift range. Observational measurements presented by VDW14 are shown as squares, with error bars representing the median and 1σ scatter. Measurements from Shen et al. (2003) are shown in the $0 < z < 0.5$ redshift bin, multiplied by 1.4 to account for the use of circularized radii (see text). The observed trends with stellar mass, redshift and galaxy type are all broadly reproduced by the simulation, as well as the extent of the scatter. The median relations found in the simulation agree with those inferred by VDW14 to within 0.1 dex for active galaxies and 0.2 dex for passive galaxies.

2.4 Galaxy classification

We distinguish between galaxies which are actively forming stars and those which are passive. The division between active and passive galaxies may be based on a cut in colour or specific star formation rate (SSFR), $\dot{M}_*/M_*$. Following Furlong et al. (2015), we apply an SSFR cut which evolves with redshift, chosen to lie approximately 1 decade below the observed main sequence of star formation at each redshift. We set the SSFR limit as $\log_{10}(\mathrm{SSFR}_{\mathrm{lim}}(z)/\mathrm{Gyr}^{-1}) = 0.5z - 2$, $z \in [0, 2]$. It was shown by Furlong et al. (2015) that the fraction of passive galaxies in the simulation is broadly consistent with observations over this redshift range. The impact of variations in the definition of active and passive galaxies on galaxy sizes is presented in Appendix D, whereas Trayford et al. (2016) show that the percentage of galaxies identified as passive is somewhat sensitive to this definition.

3 SIZE EVOLUTION OF THE GENERAL POPULATION

We begin in Section 3.1 with a comparison of the predicted size–mass relation with observations from $0 \leq z \leq 2$. The scatter in the relation is considered in Section 3.2. Having demonstrated in these sections that EAGLE reproduces the observed trends for galaxy sizes, we explore the size evolution of individual galaxies in Section 3.3 and the variation in size evolution with mass in Section 3.4.

3.1 The redshift dependence of the size–mass relation

The galaxy size–mass relation is shown in Fig. 1, with different panels showing the relation at different redshifts. In the simulation, galaxy sizes decrease with increasing redshift at a fixed stellar mass (dashed curves repeat the relations at $0 < z < 0.5$ for reference). We restrict the comparison to $z < 2$, where the sizes of simulated

galaxies typically lie above the gravitational force softening used in the simulation (indicated by horizontal dotted lines). At $z < 1$, size increases with stellar mass, with a larger increase in size per stellar mass increment above $\sim 10^{10.5}$ M$_\odot$. In the interval $1 \leq z \leq 2$, galaxy sizes show a weaker trend with stellar mass.

In each panel, the simulated galaxy sample is separated into active and passive galaxies. Passive galaxies are typically smaller than active galaxies by >0.1 dex at all redshifts for stellar masses between $10^{9.5}$ and 10^{11} M$_\odot$. At higher masses (which are sampled only at $z < 1$ by the simulation), the size–mass relations of active and passive galaxies converge. At $M_* < 10^{9.5}$ M$_\odot$, the size–mass relations of both galaxy types are also similar, but this is a consequence of limited resolution. It was shown by Schaye et al. (2015) and Furlong et al. (2015) that for $M_* < 10^{9.5}$ M$_\odot$ the SFRs of galaxies are poorly sampled compared with the higher resolution L025N0752 simulations. As a result, in this mass regime, the classification into passive and active galaxies is not robust, and the samples inevitably have similar sizes.

To compare the size–mass relations of simulated galaxies with observational constraints, we also plot the measurements of VDW14 in Fig. 1. This enables us to compare with a set of uniformly analysed observational measurements over the full redshift range. The effective radius of galaxies in the VDW14 sample is defined as the major-axis of the ellipse containing half the total flux associated with a single-component Sérsic fit applied to the 2D light profile of the galaxy. The effective radius is converted to a rest-frame wavelength of 5000 Å by empirically establishing the dependence of the radius on wavelength. We supplement the VDW14 measurements with $z = 0$ counterparts presented by Shen et al. (2003) since the limited volume of the CANDELS survey used by VDW14 precludes it from adequately sampling galaxies with $M_* > 10^{11}$ M$_\odot$ in the lowest redshift bin. Shen et al. (2003) infer the size–mass relation from SDSS (Stoughton et al. 2002) over the redshift range 0–0.3, where galaxy type is defined using concentration, Sérsic index and photometric colours. Their larger sample in this redshift bin extends the observations of the size–mass relation to $M_* \sim 10^{12}$ M$_\odot$. Note, however, that the circularized radii[2] used by Shen et al. (2003) are typically a factor of 1.4 smaller than uncircularized radii, or the major-axis radii, used by VDW14, as discussed by Dutton et al. (2011). To account for this difference, the Shen et al. (2003) sizes are multiplied by a factor of 1.4 in Fig. 1. For both active and passive galaxies, the measurements of Shen et al. (2003) and VDW14 are similar at $M_* < 10^{10.5}$ M$_\odot$, with active galaxies typically being larger than passive types of the same stellar mass for $M_* < 10^{11}$ M$_\odot$. At the higher masses probed only by Shen et al. (2003), the sizes of both types overlap. At higher redshifts, the normalization of the observed size–mass relation decreases, whereas the offset in size between the active and passive galaxies remains.

The trends seen in the simulation, namely an increase in galaxy size with stellar mass, an offset in size between active and passive galaxies, and an increasing size with decreasing redshift, are all consistent with the observed trends. Although the normalization of the size–mass relation of local galaxy disc sizes was used to calibrate the simulations, it is remarkable that the relation for active galaxies traces that of the VDW14 observations within ∼0.1 dex for all stellar masses shown up to $z = 2$. In the lowest redshift bin at $M_* > 10^{11}$ M$_\odot$ however, where no CANDELS measurements are available, there is a larger offset of ∼0.2 dex with respect to the Shen et al. (2003) data, although we note that this may be the result of the relatively bright surface brightness limit of the SDSS survey (which can be mimicked by applying a different aperture to the simulated galaxies, the effect of which is demonstrated in Appendix C). The sizes of passive galaxies are consistent with the observational measurements to within 0.1–0.2 dex, with the largest discrepancies at $M_* < 10^{9.5}$ M$_\odot$, where adequate resolution renders the definition of active and passive galaxies ambiguous. A comparison with the sizes of simulated galaxies from the ILLUSTRIS simulation (Vogelsberger et al. 2014), which are found to be a factor of 2 larger than in EAGLE and observations, is presented in Appendix A. In the following sections, we capitalize on the correspondence between EAGLE galaxies and the observational measurements to interpret the evolution of galaxy sizes in physical terms.

[2] $R_{\rm circ} = \sqrt{\frac{b}{a}} R_{\rm maj}$, where b and a are the minor- and major-axes and $R_{\rm maj}$ is the major-axis size.

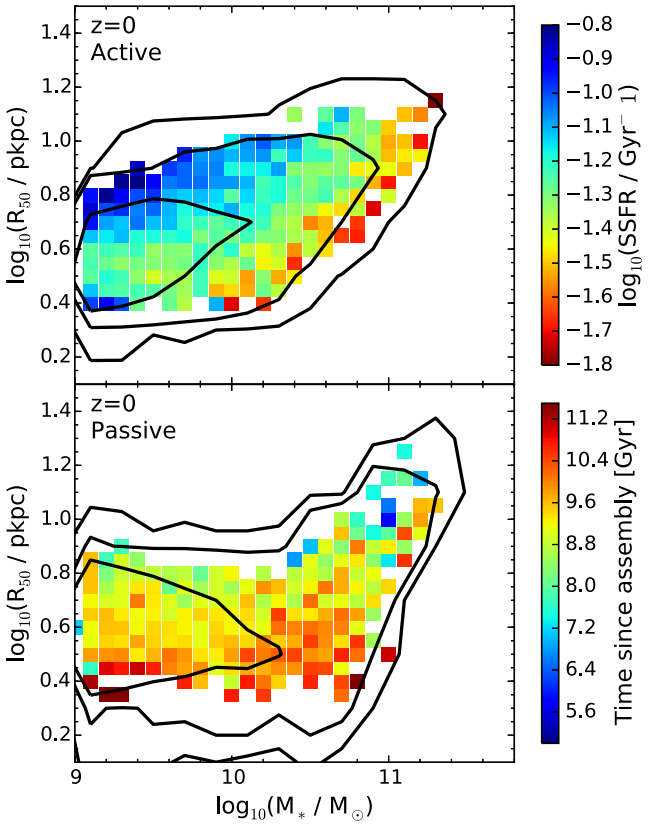

Figure 2. The $z = 0$ size–mass relations for active and passive galaxies are shown in the top and bottom panels respectively. Black contours indicate the 1, 2 and 3 sigma levels. The galaxy sizes and stellar masses are binned, with each point coloured by the median SSFR for active galaxies (upper panel) or the time since the main progenitor reached half its present-day stellar mass for passive galaxies (lower panel). There is a clear correlation between the scatter in the size–mass relation and these properties.

3.2 The scatter in the $z = 0$ size–mass relation

The scatter in the size–mass relations is quantified in Fig. 1, with an overlap in sizes between active and passive galaxies. The scatter in the observational and simulated data sets is comparable. In this section, we explore potential origins of this scatter through its correlation with other galaxy properties.

In Fig. 2, the size–mass relations at $z = 0$ for active and passive galaxies are shown in the top and bottom panels, respectively, with

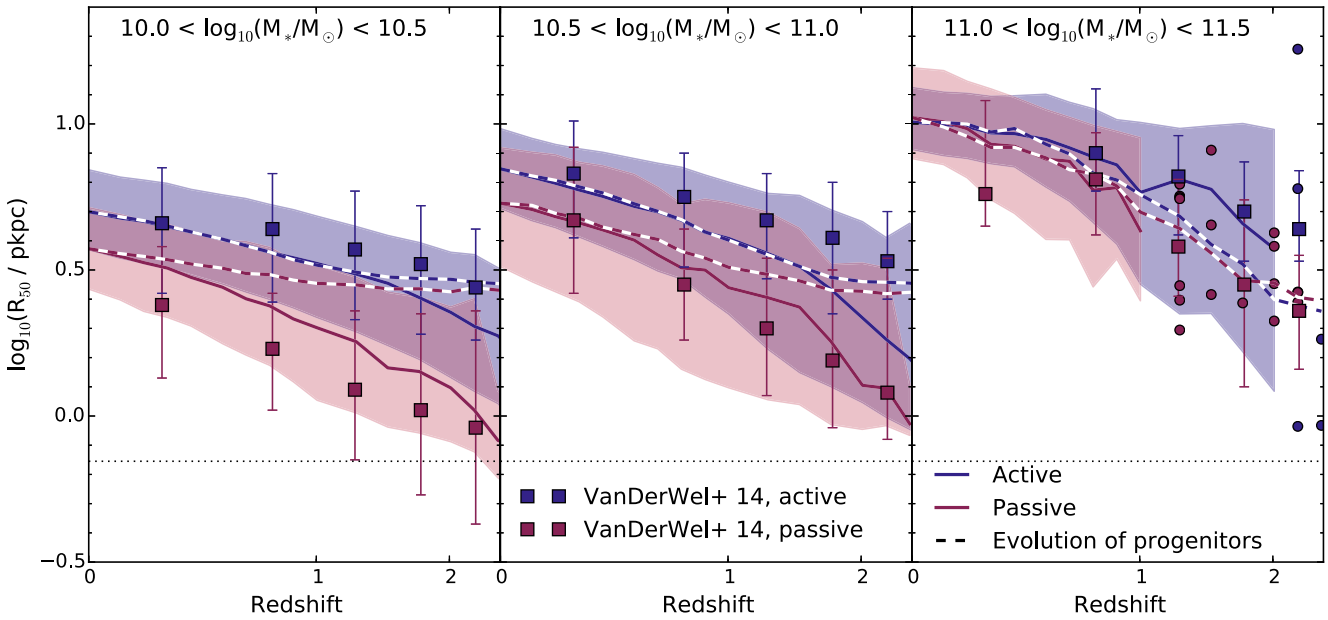

Figure 3. The evolution of the size–mass relation with redshift for active and passive galaxies in three stellar mass bins. Active and passive galaxies are shown in blue and red, respectively. The median relations from the simulation are shown by solid curves, whereas the shaded regions enclose the 16th–84th percentiles. Individual points are shown for bins containing fewer than 10 galaxies. Dashed lines show the median evolution of individual galaxies selected at redshift 0, the panel in which they appear is based on their $z = 0$ masses and the active/passive classification is based on their $z = 0$ SSFR. The evolution of individual galaxies is determined from the merger trees. Note that at $z > 0$ the galaxies used to compute the dashed curves may have a stellar mass which falls outside the range indicated in each panel and that their classification into active/passive may not correspond to the colour of the line. The horizontal dotted line corresponds to the gravitational force softening in the simulation. Measurements of the median and 1σ scatter from VDW14 are shown as squares with error bars. The redshift dependence of the size–mass relation for active galaxies is similar to the size evolution of individual active galaxies. However, this is not true for passive galaxies, owing to the evolving number density of passive galaxies.

contours showing the number density of galaxies in the size–mass plane. In the top panel, the underlying colour image shows the median SSFR of galaxies in bins of M_* and R_{50}. The figure shows a clear trend: At a fixed stellar mass, smaller galaxies have lower SSFRs.

For passive galaxies, the present-day SSFR reflects sporadic low-mass accretion, and no clear correlation between the SSFR and galaxy sizes is evident (not shown). A better measure of the past histories of passive galaxies is the time since they assembled, $t_{\rm lb,assemble}$, defined as the look-back time at which 50 per cent of the stellar mass of the $z = 0$ galaxy has assembled into a single progenitor galaxy. The bottom panel of Fig. 2 is coloured by the median value of $t_{\rm lb,assemble}$ in each bin. At a given stellar mass, smaller galaxies typically assembled earlier. A similar trend with $t_{\rm lb,assemble}$ is seen for active galaxies (not shown).

The assembly time of a galaxy reflects the assembly history of the main progenitor, and accounts for growth due to both mergers and *in situ* star formation. We have also examined the trends in the scatter with the time since formation, $t_{\rm lb,form}$, defined as the look-back time at which 50 per cent of the stellar mass in all of a galaxy's progenitors has formed, thus eliminating the contribution of growth through mergers. For passive galaxies with $M_* < 10^{10.5}$ $\rm M_\odot$, similar trends are seen for $t_{\rm lb,form}$ and $t_{\rm lb,assemble}$, but at higher masses, galaxy sizes show no clear trend with $t_{\rm lb,form}$, with all massive passive galaxies, irrespective of galaxy size, forming at similar times. For these high-mass, passive galaxies, the mergers which the galaxy has undergone must therefore play a role in the galaxy's size evolution. We will further examine the impact of mergers in Section 3.4.

3.3 The size evolution of individual galaxies

In this section, we contrast the evolution of the size of individual galaxies with the redshift dependence of the size–mass relation for the ensemble population. Naïvely, one might expect these to be equivalent. This is, however, not the case since individual galaxies evolve in mass, can switch between active and passive states, and may merge. Note that observational estimates of the size evolution of galaxies have been carried out using more sophisticated techniques such as number density matching (e.g. van Dokkum et al. 2010), which aims to account for the evolution of galaxy masses. However, accounting for the transition between active and passive states is more difficult.

In Fig. 3, the solid curves and shaded regions indicate the normalization and scatter of the size–mass relation for three bins of stellar mass at each simulation output. Note that the galaxies that fall in a particular bin can be different at each redshift due to the stellar mass evolution of individual galaxies. Comparing the sizes of galaxies over the redshift interval $z = 2$ to 0, the sizes of galaxies increase for all stellar masses, as seen in Fig. 1. The trends are similar for active and passive galaxy size–mass relations, but the very small sizes of the passive galaxy median size–mass relation at high redshifts mean that the factor by which the passive sequence increases in size is somewhat greater than for active galaxies (as quantified in Fig. 4, dashed curves). For comparison, observational data from VDW14 are represented by points with error bars; this re-emphasizes the relatively good agreement between EAGLE and observations discussed in Section 3.1.

We now compare these trends with the typical size evolution of *individual* galaxies. We select a sample of galaxies at $z = 0$

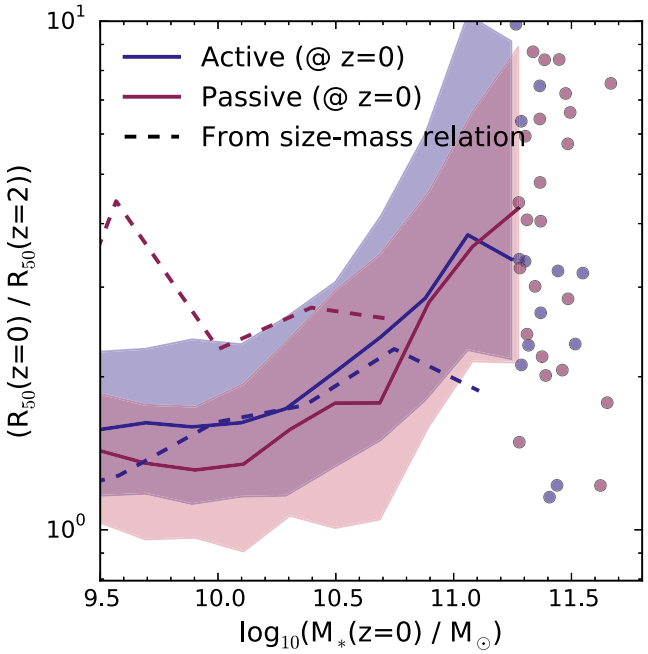

Figure 4. The size growth, $R_{50}(z=0)/R_{50}(z=2)$, from redshift 2 to 0 as a function of stellar mass. Solid lines show the median size growth from $z=2$ to 0 for individual galaxies selected based on their $z=0$ stellar mass and SSFR. Galaxies that are active and passive at $z=0$ are shown in blue and red. The size growth of these galaxies is determined based on their main progenitors at $z=2$. Individual galaxies are shown when there are fewer than 10 galaxies per stellar mass bin. The shaded regions enclose the 16th to 84th percentiles. Dashed lines show the difference in the medians of the size–mass relations at $z=2$ and $z=0$, based on the data presented in Fig. 1. Blue and red colours show the median ratios of the active and passive galaxies respectively. Note that for the dashed curves, the stellar mass plotted along the x-axis applies at both $z=2$ and 0. The size growth of individual galaxies depends strongly on $z=0$ stellar mass but only weakly on $z=0$ galaxy type. The growth determined from the redshift dependence of the size–mass relation for passive galaxies overestimates the median size growth of individual galaxies by factors of a few.

and compare the evolution of their main progenitors' sizes to the redshift dependence of the size–mass relation. We select galaxies in three $z=0$ stellar mass bins, and separate the population into active and passive types on the basis of their $z=0$ SSFRs. We then trace the galaxies back in time using the merger trees described in Section 2.2, identifying a galaxy's main progenitor at each previous simulation output. We combine the galaxies in each $z=0$ sample and overplot their median size evolution using dashed lines in Fig. 3.

It is important to note that galaxies which are passive at $z=0$ will not necessarily be passive at higher redshifts (and similarly for active galaxies – see Section 4). In fact, we see that the sizes of the samples that are active and passive at $z=0$ become similar at a higher redshift. Indeed, the comoving number density of passive galaxies at $z=2$ is less than 10 per cent of that at $z=0$, and most of the galaxies that are passive at $z=0$ were active at a high redshift. As a consequence, the sizes of the passive $z=0$ progenitors lie above the size–mass relation of high-z passive galaxies since passive galaxies are typically smaller than active galaxies at a given stellar mass. The evolution of the size–mass relation for passive galaxies is thus unlikely to reflect the evolution of individual passive galaxies. A similar conclusion was drawn by Carollo et al. (2013) based on observational measurements.

Galaxies which are selected to lie in each of the stellar mass bins at $z=0$ will generally not be in the same mass bin at a higher redshift. For example, only 3 per cent of present-day $10^{10} < M_* < 10^{10.5}$ $M_\odot$ galaxies had progenitors with stellar masses in this range at $z=2$. This results in an interesting feature in Fig. 3 at $z \geq 2$ for galaxies in the mass range of $10^{10} < M_* < 10^{11}$ $M_\odot$, where even active galaxies at this redshift are smaller by ∼0.2 dex than the progenitors of galaxies which are active and have the same mass at $z=0$. The median size–mass relation for active galaxies at $z=2$ has a shallow decrease in size with increasing stellar mass for $M_* > 10^{10}$ $M_\odot$, with a similar trend at a higher redshift; so, lower mass galaxies have larger sizes at $z \gtrsim 2$. As the progenitors of the $z=0$ sample typically have lower masses than specified in each bin at $z=2$, their sizes fall ∼0.2 dex above the median size size–mass relation.

Not only are the sizes of the progenitors of galaxies which are passive at $z=0$ similar to their active counterparts, but active and passive $z=0$ galaxies also experience broadly similar size growth. In Fig. 4, we show the size of galaxies at $z=0$ relative to the size of their main progenitor at $z=2$ (which we refer to as the size growth). The solid lines show the median ratio of the $z=2$ and 0 sizes of galaxies selected based on their $z=0$ properties, whereas the dashed lines show size growth based on the size–mass relation. Note that for the solid lines the stellar mass shown on the x-axis applies to $z=0$. For active galaxies, the size growth determined naïvely from the redshift dependence of the size–mass relation is similar to that based on individual galaxy histories, but the median size growth of individual passive galaxies is overestimated by the size–mass relation by factors of a few.

3.4 The dependence of size growth on stellar mass

It is clear from Fig. 4 that galaxy size growth from $z=2$ to 0 depends strongly on $z=0$ stellar mass. There is a strong trend with mass for both galaxy types, with the growth increasing from factors of ∼1–2 for $M_* \sim 10^{9.5}$ $M_\odot$ up to median factors of 3–4 for $M_* > 10^{11}$ $M_\odot$. This trend with $z=0$ mass is significantly more pronounced than any relation with a galaxy's $z=0$ active or passive classification, where the size growth differs only by ∼30 per cent. Given the weaker trend of the sizes with stellar mass at $z \sim 2$ relative to $z \sim 0$ in Fig. 1, a strong trend with stellar mass is anticipated.

A strong connection is expected between galaxy mergers and size growth (e.g. Cole et al. 2000; Naab, Khochfar & Burkert 2006; van der Wel et al. 2009). As will be shown by Qu et al. (2017), the number of major and minor mergers experienced by galaxies in the EAGLE simulation is a strong function of stellar mass, consistent with findings inferred from observations of close projected pairs. The correlation with $z=0$ stellar mass of both the size growth and the number of mergers since $z=2$ implies a correlation between size growth and mergers.

To examine this correlation, we consider the relation between the size growth and accreted mass fraction, where the accreted mass fraction is the ratio of stellar mass accreted since $z=2$ to the $z=0$ stellar mass. The accreted mass is defined as the contribution to the stellar mass of the galaxy from sources other than the main progenitor at a given time, where the stellar mass of the secondary branches is evaluated when these galaxies are at a radius of five times the half-mass radius of the main branch progenitor. This definition ensures that any mass lost due to stripping, before the secondary branch coalesces with the main branch, is accounted for in the accreted mass (Qu et al. 2017).

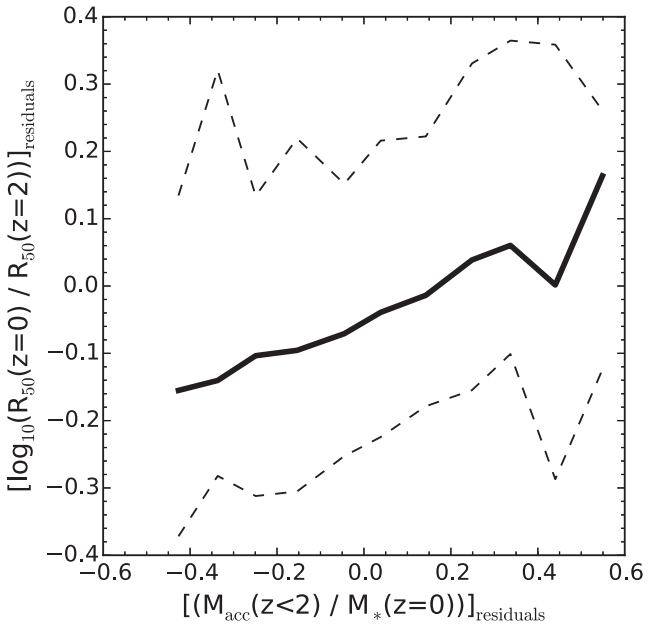

Figure 5. Residuals of the relation between size growth since $z = 2$ and stellar mass as a function of the residuals of the relation between accreted mass fraction and stellar mass. A positive correlation indicates that galaxies of a fixed stellar mass are larger if they accreted a larger fraction of their mass. The median relation is shown by the solid curve, the 16th to 84th percentiles are shown by the dashed curves. The excess in size growth correlates with an excess in accreted mass, albeit with large scatter.

We show in Fig. 5 the residuals of the size growth–M_* ($z = 0$) relation as a function of the residuals of the accreted mass fraction–M_* ($z = 0$) relation. We look at the residuals of these relations to negate the correlation of both the size growth and accreted fraction with stellar mass. In this way, we test whether size growth and accreted mass fraction are inherently related. Indeed, we see in Fig. 5 that this is the case: Excess size growth increases with an excess in accreted mass fraction. This implies that mergers directly boost size growth, beyond the stellar mass dependence of the merger rate.

In summary, we find that the growth in size of individual galaxies has a strong dependence on present-day stellar mass and a much weaker dependence on present-day galaxy classification. The merger history of a galaxy goes some of the way to explaining the dependence of size growth on $z = 0$ stellar mass; galaxies that gain more of their mass from accretion experience larger size growth.

4 SIZE EVOLUTION OF PASSIVE HIGH-REDSHIFT GALAXIES

In Section 3.1, we showed that (both in observations and in the simulation) passive galaxies at a high redshift are typically small, ∼1–2 pkpc. In the previous section, however, we saw that the main progenitors of present-day passive galaxies have sizes which are similar to the progenitors of active galaxies. This raises an obvious question: What happened to the small passive galaxies that are seen at a high redshift?

We compare the number density of passive compact galaxies to those observed in Section 4.1. We look at the evolution of all high-z passive galaxies in Section 4.2 and focus on the evolution of the compact galaxy sample in Section 4.3.

4.1 The number density of compact galaxies

Observational studies have detected massive compact red galaxies at high redshifts (e.g. Cimatti et al. 2004; Daddi et al. 2005; Trujillo et al. 2006; van Dokkum et al. 2008; Damjanov et al. 2009). The comoving number density of such galaxies is observed to increase from $z \lesssim 3$, with evidence of a turnover at $z < 1$ (VDW14; Damjanov et al. 2015).[3] Several scenarios for the evolution of this population have been proposed: Trujillo et al. (2006) suggest that the population must grow in size by factors of 3–6, for example, through dry mergers, and that the descendants today are found on the size–mass relation; van der Wel et al. (2009) similarly suggest that growth through dry mergers, combined with the continuous emergence of passive galaxies, explains the evolution of such galaxies; Poggianti et al. (2013b) suggest that at most half of the population has evolved appreciably in size based on the luminosity-weighted ages of present-day compact galaxies; Graham, Dullo & Savorgnan (2015) conclude that the high-z compact galaxies may simply be the compact cores of local early-type disc galaxies today.

We begin our analysis by defining our compact galaxy selection as that which is passive with $(R_{50}/\mathrm{pkpc})/(M_*/10^{11}\ \mathrm{M}_\odot)^{0.75} < 2.5$, following VDW14. The evolution of the number density of passive galaxies satisfying the compactness criteria in the simulation is shown in Fig. 6. Applying the same conditions as those applied to the VDW14 sample, namely that galaxies are red/passive and have $M_* > 10^{10.5}\ \mathrm{M}_\odot$ (solid curve), a reasonably flat number density evolution is recovered from $z = 2$ to 0.5, with a decline for $z < 0.5$. Relaxing the mass constraint to include all galaxies with $M_* > 10^{10}\ \mathrm{M}_\odot$ increases the number density of galaxies identified but does not change the overall evolutionary trend (dashed curve).

Compared with the observations of VDW14, also shown in Fig. 6, the number density of compact galaxies in the simulation is too low, although there is a similar turnover at a low redshift. Recently, the theoretical study of Wellons et al. (2015a) considered the evolution of compact galaxies identified in the ILLUSTRIS simulation, using the Barro et al. (2013) criterion for compactness (transformed to a 3D radius), $R_{50}/(M_*/10^{11}\ \mathrm{M}_\odot)^{0.75} < 4.5$. Adopting this more relaxed definition of compactness significantly increases the number of compact galaxies, and the ILLUSTRIS simulation generates a similar abundance of compact galaxies to the EAGLE simulation.

The discrepancy with the observations of VDW14 is at least in part due to the limited box size of the simulation. Indeed, comparing with a simulation in a smaller box of 50^3 cMpc^3 (with the same resolution and subgrid physics as in Ref-L100N1504), no compact galaxies are found with $M_* > 10^{10.5}\ \mathrm{M}_\odot$, implying an upper limit to the number density of 8×10^{-6} cMpc^{-3}, significantly lower than the 3×10^{-5} cMpc^{-3} found at $1.5 \gtrsim z \gtrsim 2$ for our fiducial simulation. Thus, it is clear that compact galaxies tend to form in the large-scale overdensities which are poorly sampled, even in the $(100\,\mathrm{cMpc})^3$ volume of the Eagle simulation. Indeed, 10 out of the 24 compact galaxies studied below are located in the 6 most massive haloes in the simulation at $z =$ (see also Wellons et al. 2015a). A strong dependency on large-scale structure is also consistent with the observation that present-day compact galaxies are preferentially found in galaxy clusters (Poggianti et al. 2013a). The galaxies which are found in the simulation are therefore very likely to be representative of compact galaxies identified in the real Universe.

[3] The existence of a turnover depends on the definition of 'compact' (see Damjanov et al. 2015 for a comparison of different selection criteria in the literature).

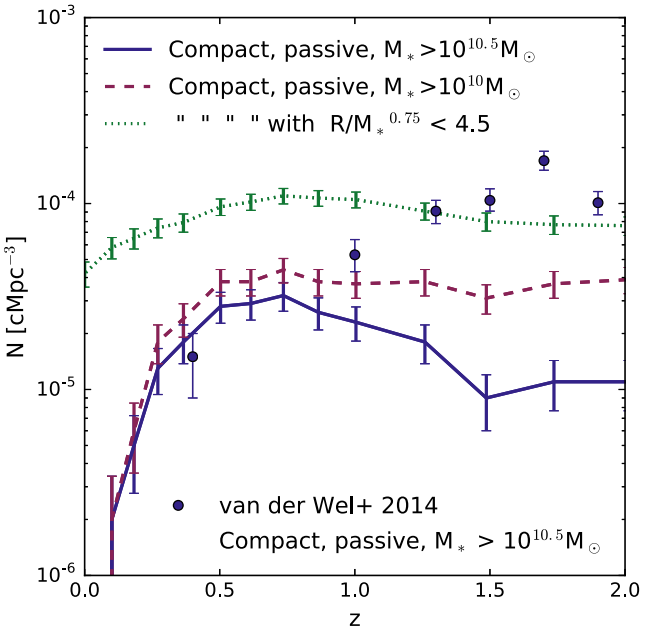

Figure 6. The comoving number density of compact galaxies in the simulation as a function of redshift, where compact galaxies are those with $R_{50}/(M_*/10^{11}\ \mathrm{M}_\odot)^{0.75} < 2.5$ pkpc, as defined by VDW14. The blue solid curve shows compact galaxies which are passive and have $M_* > 10^{10.5}$ $\mathrm{M}_\odot$, and the red dashed curve lowers the mass limit to $M_* > 10^{10}$ $\mathrm{M}_\odot$. Error bars on the simulation data indicate the Poisson error per redshift bin. The observational measurements of VDW14 are shown as points with 1σ error bars. Many massive compact galaxies are identified in the simulation; however, the number density falls below that of the observations at $z \geq 1$, which is, at least, in part due to the limited box size of the simulation. In green, we show the number density of $M_* > 10^{10}$ $\mathrm{M}_\odot$ compact galaxies matching the less stringent criterion, $R_{50}/(M_*/10^{11}\ \mathrm{M}_\odot)^{0.75} < 4.5$ pkpc, used by Barro et al. (2013) and Wellons et al. (2015a). The abundance of galaxies increases sharply as the compactness criterion is relaxed.

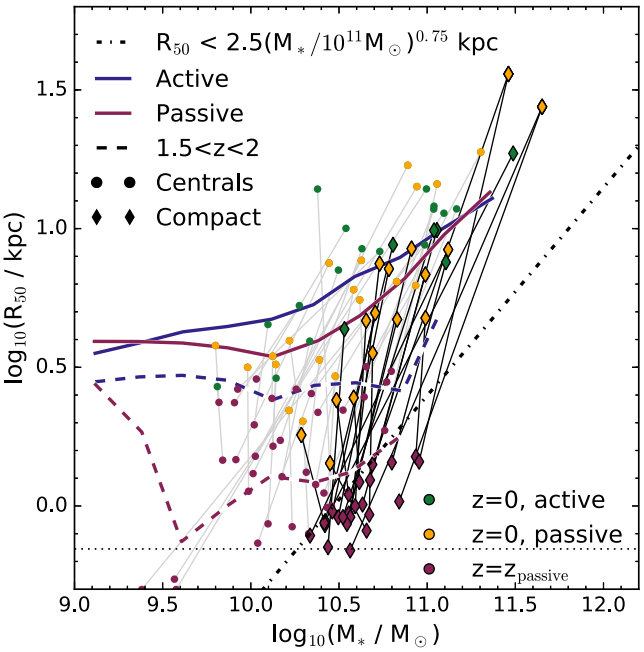

Figure 7. The evolution of galaxies which are passive in the redshift range $1.5 < z < 2$ and centrals at $z = 0$ in the size–stellar mass plane from the redshift where they are first identified as passive, z_{passive}, to $z = 0$. Points at z_{passive} are shown in red, whereas redshift 0 points are coloured by galaxy type, where orange indicates passive galaxies at $z = 0$ and green indicates active galaxies at $z = 0$. A grey line connects the $z = z_{\mathrm{passive}}$ and $z = 0$ points for each galaxy. Any galaxy lying to the right-hand side of the dash–dotted line is defined as compact. For the compact galaxies, the evolution is highlighted using black lines and diamond symbols. (Note that all compact galaxies are shown, not only those which are centrals at $z = 0$.) The median size–mass relations for active (blue) and passive (red) galaxies are shown at $z = 0$, and for the range $1 < z < 2$, as solid and dashed lines, respectively. The horizontal dotted line corresponds to the simulation gravitational softening. All compact galaxies increase in size by at least 0.2 dex from when they were first identified as passive, and similar for all centrals. None of the high-z compact galaxies remains compact to $z = 0$. Although all galaxies shown are passive in the interval $1.5 < z < 2$, not all are passive at $z = 0$.

4.2 The destiny of high-z passive galaxies

As already noted, the typical evolution of all high-z passive galaxies cannot be understood from the evolutionary histories of the passive $z = 0$ galaxy sample considered in Section 3.3. However, restricting the analysis to galaxies which satisfy the compact galaxy criteria excludes many of the high-z passive galaxies due to its strong dependence on stellar mass (see dot–dashed curve in Fig. 7). In the following analysis, we consider the evolution of all high-z passive galaxies, not only those which are compact, but we emphasize the evolution of the compact subsample.

We select all galaxies which are identified as passive in at least one output in the redshift range $1.5 < z < 2$ (corresponding to the bottom right-hand panel of Fig. 1). We ensure that no galaxy is double counted if identified as passive in multiple outputs in this redshift range by ensuring that we include only the highest redshift galaxy identified as passive on any tree branch. We identify 331 high-z passive galaxies among the ∼10 000 galaxies with $M_* > 10^9$ $\mathrm{M}_\odot$ in this redshift range.[4] Of the 331 galaxies, 44 galaxies are and remain the central galaxies of their halo until $z = 0$, and 83 are or become satellite galaxies by $z = 0$, while the remaining 204 merge with a more massive galaxy.[5] Focusing specifically on compact high-z passive galaxies, 24 of the 331 are compact at $1.5 < z < 2$, 9 are centrals at $z = 0$, 7 are satellites and the remaining 8 are merged into other systems. With over 60 per cent of all high-z passive galaxies and ∼50 per cent of compact galaxies merged with more massive systems by $z = 0$, the size evolution of their descendant is not set primarily by the properties of the passive or compact galaxy, thus rendering these properties largely inconsequential to the $z = 0$ population.

Fig. 7 shows the evolution of the high-z passive galaxies in the size–mass plane for the central and compact selections. All galaxies from the central high-z passive population increase in size between $z = 2$ and 0, with most galaxies also increasing in mass. The resulting $z = 0$ descendants have grown towards the present-day size–mass relation. Although these galaxies were selected to be passive in at least one output in the range $1.5 < z < 2$, of the 44 galaxies, 25 are active at the present day (green symbols).

The growth of the compact galaxy selection is highlighted in Fig. 7 using diamond symbols and black lines. These galaxies follow

[4] The number of galaxies with $M_* > 10^9$ $\mathrm{M}_\odot$ increases from 7980 at $z = 2$ to 10 510 at $z = 1.5$ due to the formation and mass growth of galaxies.

[5] If a galaxy is not on the main branch of a $z = 0$ galaxy, it is considered to have merged with a more massive system.

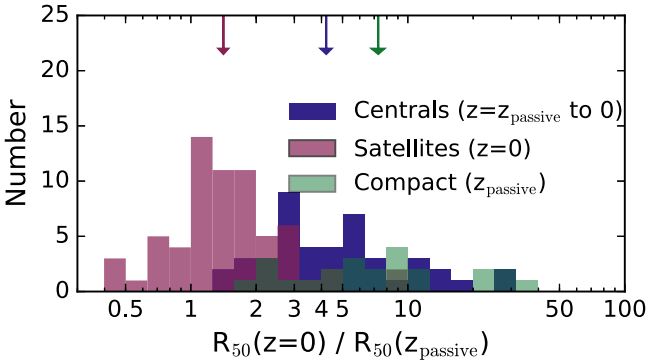

Figure 8. The distribution of the relative size growth for high-z passive galaxies between the highest redshift in the range $1.5 < z < 2$ at which they are identified as passive and $z = 0$. Galaxies which remain centrals until $z = 0$ are shown in blue, whereas $z = 0$ satellites are shown in red. The compact galaxies highlighted in Fig. 7 are shown in green, which include centrals, satellites and merged galaxies. The median size growth of each sample is indicated by an arrow. All galaxies show broad distributions in size growth, with several satellite galaxies decreasing in size.

the trends of the central population, typically growing in both mass and size, with some experiencing renewed star formation. Note that none remains compact until $z = 0$.

A histogram of the size growth for centrals, satellites and compact galaxies is shown in Fig. 8. The high-z passive galaxies which remain as centrals to $z = 0$ increase in size with a median size growth of a factor of 4; the growth ranges from ∼2 to 30. Galaxies which are identified as satellites at $z = 2$ undergo a variety of size growth scenarios; some of these galaxies increase in size by up to a factor of 10, whereas others decrease in size, with a median size growth of ∼1. A decrease in galaxy size can result from environmental processes, such as stripping and harassment (Moore et al. 1996), experienced by galaxies in dense environments. The compact galaxies, which include centrals, satellites and merged systems, all increase in size, by factors of ∼2 to 40, although those experiencing size growth >20 have been merged with a more massive system, and would not be counted as its main progenitor.

4.3 Growth mechanisms of compact galaxies

We extend the analysis of the compact galaxies to consider how they grow. In Fig. 9, we show the radial profile of three example galaxies, chosen to illustrate different growth mechanisms. The left-hand panels show the distribution of the star particles at $z = 2$, and of the same particles at $z = 0$. In all cases, the stars migrate radially outwards. The red and yellow arrows compare the half-mass radii of these stars at $z = 0$ and 2, respectively. The half-mass radii of the galaxies at $z = 0$ are indicated by a blue arrow. Comparing the yellow and blue arrows shows how much of the total size growth is due to the migration of $z = 2$ stars relative to other sources of size growth such as accretion or *in situ* star formation. The right-hand panel shows the radial distributions of stars formed since $z = 2$, with those formed in the main progenitor of the galaxy highlighted in green. Fig. 10 shows images of these three galaxies at $z = 0$ in edge-on and face-on projections.

The top panels show a galaxy whose size growth can almost entirely be accounted for by the radial migration of its $z = 2$ star particles. The half-mass radius of $z = 2$ stars at $z = 0$, $R_{50,\,\mathrm{stars}(z=2)}(z = 0)$, is approximately equal to $R_{50}(z = 0)$ (yellow and blue arrows, respectively). The star particles added to the system at $z < 2$, shown

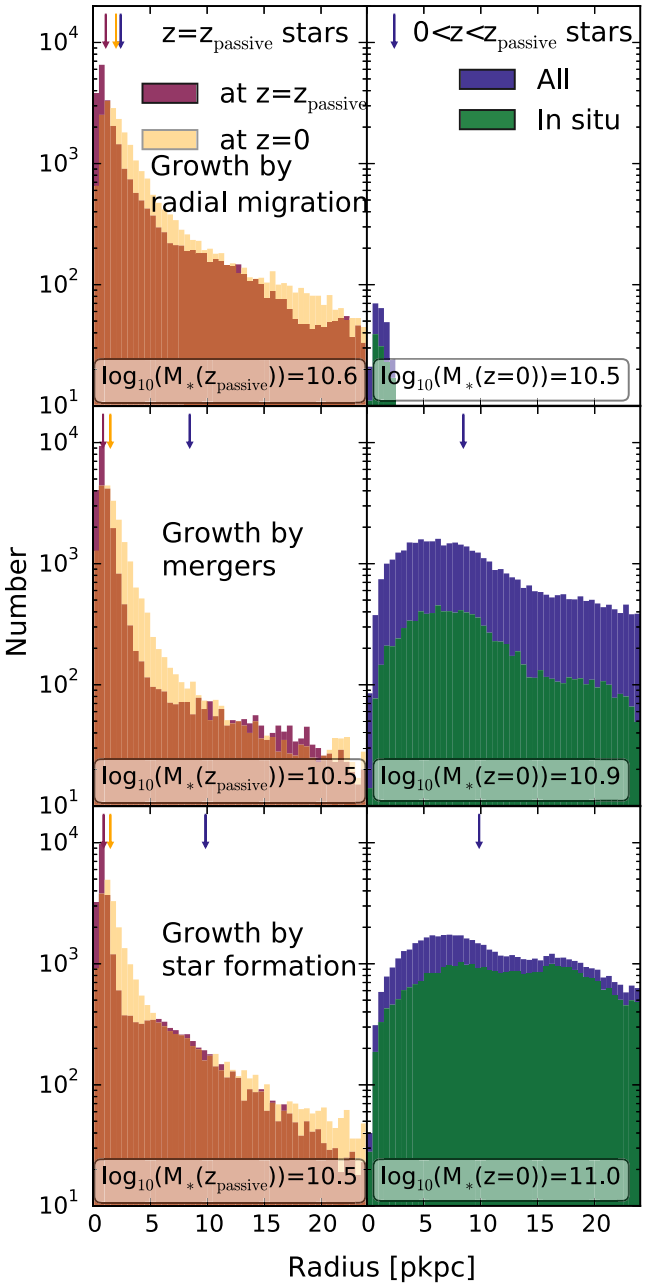

Figure 9. The radial distributions of star particles in three example galaxies. In the left-hand panels, red histograms show the distribution of star particles in the galaxy at $z = 2$, whereas the yellow histograms show the distributions of the same star particles at $z = 0$. In the right-hand panels, all other star particles in the $z = 0$ galaxies are shown in blue. Those which formed *in situ* are shown in green. The scales in the panels are the same, enabling a direct comparison of the numbers of star particles of each type. The sizes of the galaxies at $z = 2$ (0) are shown as red (blue) arrows. The yellow arrows show the half-mass radii of the $z = 2$ star particles at $z = 0$. In all cases, the $z = 2$ star particles have migrated to larger radii by $z = 0$, resulting in modest size growth. Further size growth is contributed by accreted stars in the middle panels and by *in situ* formation of stars in the lower panels.

in the right-hand panel, contribute less than 10 per cent of the $z = 0$ stellar mass and are centrally concentrated. The galaxy undergoes a period of rapid black hole growth, shortly after it is selected, which suppresses its SFR. It then soon falls into a larger halo where its star formation is quenched. In this case, the galaxy's size growth

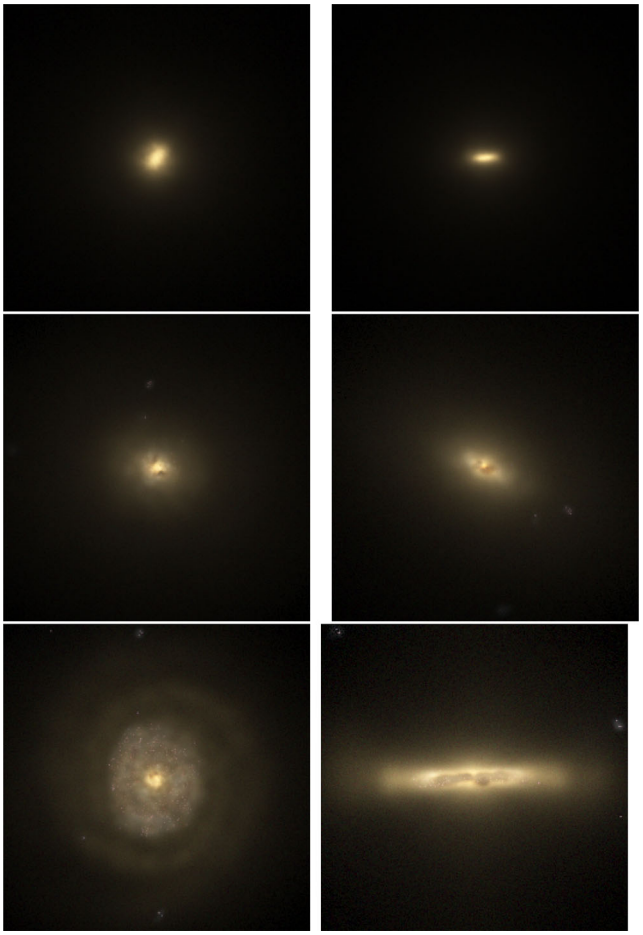

Figure 10. Images of galaxies from Fig. 9 at $z = 0$ in face-on and edge-on. The top, middle and bottom rows correspond to the galaxies shown in the top, middle and bottom rows of Fig. 9, respectively. The images were produced using the radiative transfer code SKIRT (Baes et al. 2011) applied to EAGLE galaxies, as described in Trayford et al. (2016). Stellar light in *g*, *r* and *i*-band SDSS filters is shown, with dust attenuation. Images are shown in thumbnails of 60 pkpc per side. The galaxy in the top row increases in size due to the redistribution of its $z = 2$ stars, the middle row galaxy grows by a larger factor due to accreted stellar mass, while the bottom row galaxy experiences renewed star formation in the outskirts of the galaxy forming at disc at $z = 0$.

is modest. Since we use a conservative gravitational softening in the simulation, the growth which occurs is not likely to be driven by a discretization effect, and external drivers such as the fly-by encounters experienced a cluster environment are more likely to be responsible.

The middle panels show a system where $R_{50,\,\mathrm{stars}(z=2)}(z = 0) \ll R_{50}(z = 0)$. The origin of the additional growth in size of this system can be understood from the right-hand panel. In this galaxy, many star particles have been accreted (difference between blue and green histograms), particularly at large radii, driving the size growth. The accreted particles account for ∼40 per cent of $M_*\,(z = 0)$, with stars formed *in situ* accounting for a further ∼20 per cent and $z = 2$ star particles (after accounting for stellar mass-loss) accounting for the remaining 40 per cent. The accreted stars do not dominate the stellar mass, but their radial distribution significantly increases the half-mass radius.

Not all galaxies with $R_{50,\,\mathrm{stars}(z=2)}(z = 0) \ll R_{50}(z = 0)$ grow to their $z = 0$ sizes due to accretion and mergers. In some cases, star formation is a major contributor, as seen in the bottom panels of Fig. 9. This star formation may be triggered by mergers, but the stars were formed *in situ*. Note that we cannot tell from this plot whether the stars formed at large radii or whether they migrated outwards after their formation. However, images of this galaxy at $z = 0$, as seen in the bottom panel of Fig. 10, indicate that a disc of recently formed stars is in place in the outskirts of the galaxy.

It is evident from the simulation that the growth mechanisms of compact galaxies are diverse. All compact galaxies increase in size, but some grow only through radial migration, limiting their size growth to factors of ∼2, whereas others grow through mergers and/or renewed star formation, where the compact galaxy progenitor can be found at the core of the $z = 0$ descendant. However, over 50 per cent of the compact galaxies identified at $z \sim 2$ have merged into more massive systems by $z = 0$, and their $z = 0$ descendants therefore do not obviously reflect the compact galaxies' histories.

It is worthwhile to pause and consider whether the results we have found in the simulation are applicable to the real Universe. While the simulation provides a good description of a great many properties of galaxies, we have seen that it significantly underpredicts the abundance of compact galaxies at $z > 1$. It is very likely that this is because the compact population is associated with regions of high overdensity which later collapse to form galaxy clusters. Such regions are poorly sampled in the finite simulation volume: Only six systems with dark matter halo mass greater than 10^{14} $\mathrm{M}_\odot$ are present in the volume at $z = 0$. With this caveat, we believe that the histories of compact galaxies in the simulation are representative of those in the observable Universe.

In summary, 60 per cent of the high-z passive galaxies merge into more massive systems by $z = 0$, 25 per cent survive as satellites to $z = 0$ and the remaining 15 per cent are centrals at $z = 0$. Most centrals and ∼50 per cent of the satellites which survive to $z = 0$ increase in size with many of the centrals experiencing renewed star formation. The compact sample of the high-z passive galaxies undergoes size growth up to a factor of ∼40, growing through stellar migration (which, however, yields only modest size growth), renewed star formation and mergers.

5 SUMMARY AND CONCLUSIONS

We have studied the evolution of the galaxy size–mass relation in the EAGLE cosmological hydrodynamical simulation, distinguishing between actively star forming and passive galaxy populations. By comparing the half-mass radii from the simulation with the sizes inferred from the observations of VDW14, we arrive at the following results (Figs 1 and 3):

(i) The dependence of the sizes of simulated galaxies on stellar mass, redshift and star formation classification is close to that of observed galaxies. Galaxy sizes typically increase with stellar mass and decreasing redshift, and active galaxies are typically larger than their passive counterparts at a given stellar mass.

(ii) The level of agreement between the predicted and observed sizes is of the order of 0.1–0.2 dex below 10^{11} $\mathrm{M}_\odot$ (equivalent to 1–2 pkpc) for $0 \leq z \leq 2$.

(iii) The scatter in the sizes at a given mass is also similar in simulated and observed galaxies.

Since the simulation agrees relatively well with the observational data, we used the simulation as a tool to explore the size evolution of galaxy populations. Our conclusions are as follows:

(i) We find that the scatter in the size–mass relation correlates well with the SSFR for active galaxies and with the time since assembly for passive galaxies (Fig. 2). Active galaxies of a given mass with higher SSFRs are typically larger. Similarly, passive galaxies at a given stellar mass which assembled more recently are larger than those which formed earlier. This result contrasts with the semi-analytic model of Dutton, van den Bosch & Dekel (2010), which predicts that variations in halo spin will drive galaxies along the SFR sequence.

(ii) We compared the evolution of star-forming and passive galaxies as determined from the redshift dependence of the size–mass relation of the ensemble population (which can be accessed directly by observations) and the typical size evolution of individual galaxies based on their main progenitors (which can be traced explicitly in simulations through galaxy merger trees). For galaxies that are active at $z = 0$, the evolution of the size–mass relation for the population is similar to the typical evolution of individual objects. However, in contrast to the rapid evolution of the size–mass relation for the population of passive galaxies, the size evolution of individual present-day passive galaxies is comparable to that of their star-forming counterparts (Figs 3 and 4). This difference arises simply because most present-day passive galaxies were star forming at higher redshifts (e.g. van Dokkum & Franx 1996).

(iii) The relative growth of galaxy sizes from $z = 2$ to 0 increases strongly with present-day stellar mass (Fig. 4). This dependence is partly due to the influence of galaxy mergers on sizes: Galaxies with a higher fraction of accreted mass relative to the median at a fixed mass experience an excess in size growth (Fig. 5). This result has previously been demonstrated using simulations of individual early-type galaxies (e.g. Oser et al. 2010).

(iv) We investigated the evolution of 313 galaxies identified as passive in at least one output in the redshift range $1.5 < z < 2$. Of these galaxies, 65 per cent merge into more massive objects by $z = 0$, 26 per cent are satellites and 14 per cent are centrals at $z = 0$. Satellite galaxies experience diverse size growth, with many decreasing in both size and mass most likely due to environmental processes such as tidal stripping. The central galaxies all increase in size between $z = 2$ and 0, and at $z = 0$, they are found to lie near the present-day size–mass relations for the general population. In ∼50 per cent of central galaxy cases, they experience renewed star formation, indicating that instantaneous passive identification at high z is not indicative of a galaxy's future evolution. These results are in agreement with the picture that is emerging from studies of observational samples (e.g. van Dokkum et al. 2015).

(v) Of the high-z passive galaxies, 24 were identified as compact using the criterion of VDW14. Of these galaxies, eight merge with more massive systems, seven are satellites and nine are centrals at $z = 0$. For all compact galaxies, the stars formed at $z = 2$ migrate to somewhat larger radii by $z = 0$. In the cases where further growth occurs due to mergers and star formation, the driver of the growth depends on the radial distribution of stars added to the galaxy at a lower redshift and thus on the angular momentum gained by the parent halo. A more detailed comparison of the evolution of halo angular momentum and its relation to the spin of galaxies can be found in Zavala et al. (2016).

The EAGLE simulation appears to reproduce many aspects of the observable Universe, in particular, the stellar mass distribution and sizes of galaxies in the local Universe. It is thus an ideal tool for understanding the drivers of size growth. However, we caution that the sizes of the smallest galaxies (<1 pkpc) may be set by the polytropic equation of state which is imposed on the unresolved ISM. Higher resolution simulations which include the physics required to model the cold interstellar gas phase are required to make further progress on galaxies in this regime, and thus to extend our results to higher redshifts.

ACKNOWLEDGEMENTS

This work used the DiRAC Data Centric system at Durham University, operated by the Institute for Computational Cosmology on behalf of the STFC DiRAC HPC Facility (www.dirac.ac.uk). This equipment was funded by BIS National E-infrastructure capital grant ST/K00042X/1, STFC capital grant ST/H008519/1, and STFC DiRAC Operations grant ST/K003267/1 and Durham University. DiRAC is part of the National E-Infrastructure. We also gratefully acknowledge PRACE for awarding us access to the resource Curie based in France at Trés Grand Centre de Calcul. This work was sponsored by the Dutch National Computing Facilities Foundation (NCF) for the use of supercomputer facilities, with financial support from the Netherlands Organization for Scientific Research (NWO).

RAC is a Royal Society University Research Fellow. The research was supported in part by the Interuniversity Attraction Poles Programme initiated by the Belgian Science Policy OWNce ([AP P7/08 CHARM]), in part by the National Science Foundation under Grant No. NSF PHY11-25915, in part by the UK Science and Technology Facilities Council (grant numbers ST/F001166/1 and ST/I000976/1), and in part by the Rolling and Consolidating Grants to the ICC, Marie Curie Reintegration Grant PERG06-GA-2009-256573 and ERC grant agreement 278594-GasAroundGalaxies.

REFERENCES

Aumer M., White S. D. M., Naab T., Scannapieco C., 2013, MNRAS, 434, 3142
Baes M., Verstappen J., De Looze I., Fritz J., Saftly W., Vidal Pérez E., Stalevski M., Valcke S., 2011, ApJS, 196, 22
Bahé Y. M. et al., 2016, MNRAS, 456, 1115
Baldry I. K. et al., 2012, MNRAS, 421, 621
Barro G. et al., 2013, ApJ, 765, 104
Bezanson R., van Dokkum P. G., Tal T., Marchesini D., Kriek M., Franx M., Coppi P., 2009, ApJ, 697, 1290
Brook C. B. et al., 2011, MNRAS, 415, 1051
Brook C. B., Stinson G., Gibson B. K., Roškar R., Wadsley J., Quinn T., 2012a, MNRAS, 419, 771
Brook C. B., Stinson G., Gibson B. K., Wadsley J., Quinn T., 2012b, MNRAS, 424, 1275
Bruzual G., Charlot S., 2003, MNRAS, 344, 1000
Carollo C. M. et al., 2013, ApJ, 773, 112
Chabrier G., 2003, PASP, 115, 763
Charlot S., Fall S. M., 2000, ApJ, 539, 718
Cimatti A. et al., 2004, Nature, 430, 184
Cole S., Lacey C. G., Baugh C. M., Frenk C. S., 2000, MNRAS, 319, 168
Crain R. A. et al., 2009, MNRAS, 399, 1773
Crain R. A. et al., 2015, MNRAS, 450, 1937
Daddi E. et al., 2005, ApJ, 626, 680
Dalla Vecchia C., Schaye J., 2012, MNRAS, 426, 140
Damjanov I. et al., 2009, ApJ, 695, 101
Damjanov I., Geller M. J., Zahid H. J., Hwang H. S., 2015, ApJ, 806, 158
De Lucia G., Blaizot J., 2007, MNRAS, 375, 2
Dehnen W., Aly H., 2012, MNRAS, 425, 1068
Dolag K., Borgani S., Murante G., Springel V., 2009, MNRAS, 399, 497
Durier F., Dalla Vecchia C., 2012, MNRAS, 419, 465

Dutton A. A., van den Bosch F. C., Dekel A., 2010, MNRAS, 405, 1690
Dutton A. A. et al., 2011, MNRAS, 410, 1660
Fall S. M., Efstathiou G., 1980, MNRAS, 193, 189
Ferland G. J., Korista K. T., Verner D. A., Ferguson J. W., Kingdon J. B., Verner E. M., 1998, PASP, 110, 761
Furlong M. et al., 2015, MNRAS, 450, 4486
Governato F. et al., 2004, ApJ, 607, 688
Graham A. W., Dullo B. T., Savorgnan G. A. D., 2015, ApJ, 804, 32
Haardt F., Madau P., 2001, in Neumann D. M., Tran J. T. V., eds, XXIst Moriond Astrophys. Meeting, Clusters of Galaxies and the High Redshift Universe Observed in X-rays. Editions Frontieres, Paris, p. 64
Head J. T. C. G., Lucey J. R., Hudson M. J., 2015, MNRAS, 453, 3729
Hilz M., Naab T., Ostriker J. P., 2013, MNRAS, 429, 2924
Hopkins P. F., 2013, MNRAS, 428, 2840
Hopkins P. F., Bundy K., Hernquist L., Wuyts S., Cox T. J., 2010, MNRAS, 401, 1099
Hopkins P. F., Kereš D., Oñorbe J., Faucher-Giguère C.-A., Quataert E., Murray N., Bullock J. S., 2014, MNRAS, 445, 581
Jenkins A., 2010, MNRAS, 403, 1859
Jiang L., Helly J. C., Cole S., Frenk C. S., 2014, MNRAS, 440, 2115
Katz N., Gunn J. E., 1991, ApJ, 377, 365
Kelvin L. S. et al., 2012, MNRAS, 421, 1007
Kennicutt Jr. R. C., 1998, ApJ, 498, 541
Lagos C. d. P. et al., 2015, MNRAS, 452, 3815
Lange R. et al., 2015, MNRAS, 447, 2603
McAlpine S. et al., 2016, Astron. Comput., 15, 72
McCarthy I. G., Schaye J., Font A. S., Theuns T., Frenk C. S., Crain R. A., Dalla Vecchia C., 2012, MNRAS, 427, 379
Marinacci F., Pakmor R., Springel V., 2014, MNRAS, 437, 1750
Mo H. J., Mao S., White S. D. M., 1998, MNRAS, 295, 319
Moore B., Katz N., Lake G., Dressler A., Oemler A., 1996, Nature, 379, 613
Munshi F. et al., 2013, ApJ, 766, 56
Muzzin A. et al., 2013, ApJ, 777, 18
Naab T., Khochfar S., Burkert A., 2006, ApJ, 636, L81
Naab T., Johansson P. H., Ostriker J. P., 2009, ApJ, 699, L178
Navarro J. F., White S. D. M., 1994, MNRAS, 267, 401
Nelson D. et al., 2015, Astron. Comput., 13, 12
Okamoto S., Millis A. J., 2005, Phys. Rev. B, 72, 235108
Oser L., Ostriker J. P., Naab T., Johansson P. H., Burkert A., 2010, ApJ, 725, 2312
Oser L., Naab T., Ostriker J. P., Johansson P. H., 2012, ApJ, 744, 63
Patel S. G. et al., 2013, ApJ, 766, 15
Planck Collaboration XVI, 2014, A&A, 571, A16
Poggianti B. M. et al., 2013a, ApJ, 762, 77
Poggianti B. M., Moretti A., Calvi R., D'Onofrio M., Valentinuzzi T., Fritz J., Renzini A., 2013b, ApJ, 777, 125
Qu Y. et al., 2017, MNRAS, 464, 1659
Rahmati A., Schaye J., Bower R. G., Crain R. A., Furlong M., Schaller M., Theuns T., 2015, MNRAS, 452, 2034
Rosas-Guevara Y. M. et al., 2016, MNRAS, 462, 190
Sales L. V., Navarro J. F., Schaye J., Dalla Vecchia C., Springel V., Booth C. M., 2010, MNRAS, 409, 1541
Scannapieco C. et al., 2012, MNRAS, 423, 1726
Schaller M., Dalla Vecchia C., Schaye J., Bower R. G., Theuns T., Crain R. A., Furlong M., McCarthy I. G., 2015a, MNRAS, 454, 2277
Schaller M. et al., 2015b, MNRAS, 451, 1247
Schaye J., Dalla Vecchia C., 2008, MNRAS, 383, 1210
Schaye J. et al., 2010, MNRAS, 402, 1536
Schaye J. et al., 2015, MNRAS, 446, 521
Shen S., Mo H. J., White S. D. M., Blanton M. R., Kauffmann G., Voges W., Brinkmann J., Csabai I., 2003, MNRAS, 343, 978
Snyder G. F., Lotz J. M., Rodriguez-Gomez V., da Silva Guimaraes R., Torrey P., Hernquist L., 2016, MNRAS, preprint (arXiv:1610.01156)
Springel V., 2005, MNRAS, 364, 1105
Springel V., White S. D. M., Tormen G., Kauffmann G., 2001, MNRAS, 328, 726
Springel V., Di Matteo T., Hernquist L., 2005, MNRAS, 361, 776
Stoughton C. et al., 2002, AJ, 123, 485
Torrey P. et al., 2015, MNRAS, 447, 2753
Trayford J. W. et al., 2015, MNRAS, 452, 2879
Trayford J. W., Theuns T., Bower R. G., Crain R. A., Lagos C. d. P., Schaller M., Schaye J., 2016, MNRAS, 460, 3925
Trujillo I. et al., 2006, MNRAS, 373, L36
van der Wel A., Rix H.-W., Holden B. P., Bell E. F., Robaina A. R., 2009, ApJ, 706, L120
van der Wel A. et al., 2014, ApJ, 788, 28 (VDW14)
van Dokkum P. G., Franx M., 1996, MNRAS, 281, 985
van Dokkum P. G. et al., 2008, ApJ, 677, L5
van Dokkum P. G. et al., 2010, ApJ, 709, 1018
van Dokkum P. G. et al., 2014, ApJ, 791, 45
van Dokkum P. G. et al., 2015, ApJ, 813, 23
Vogelsberger M. et al., 2014, MNRAS, 444, 1518
Wellons S. et al., 2015a, MNRAS, 449, 361
Wellons S. et al., 2015b, MNRAS, 449, 361
Wendland H., 1995, Adv. Comput. Math., 4, 389
White S. D. M., Frenk C. S., 1991, ApJ, 379, 52
White S. D. M., Rees M. J., 1978, MNRAS, 183, 341
Wiersma R. P. C., Schaye J., Smith B. D., 2009a, MNRAS, 393, 99
Wiersma R. P. C., Schaye J., Theuns T., Dalla Vecchia C., Tornatore L., 2009b, MNRAS, 399, 574
Zavala J. et al., 2016, MNRAS, 460, 4466

APPENDIX A: COMPARISON WITH OTHER SIMULATIONS

In Fig. A1, the size–mass relations from the EAGLE and ILLUSTRIS galaxy formation simulations are compared in four redshift bins between 0 and 2, separating each galaxy population into active and passive galaxies using the SSFR cut described in Section 2.4. The EAGLE simulation is as shown in Fig. 1. For ILLUSTRIS (Vogelsberger et al. 2014), the half-mass radii, stellar masses and SFRs were obtained from their public data release (Nelson et al. 2015). An aperture of twice the half-mass radius is used to measure the stellar masses and SFRs, as was applied in previous ILLUSTRIS publications.

For both hydrodynamical simulations, galaxy sizes tend to increase with stellar mass, and there is an offset between the sizes

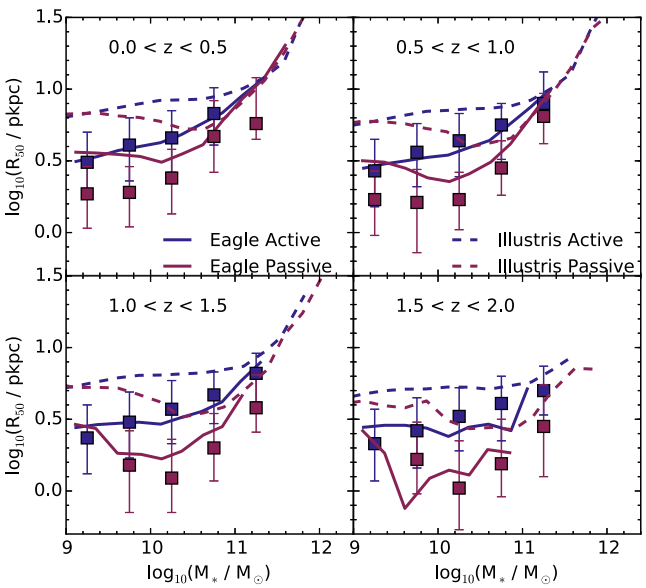

Figure A1. The median size–mass relation from EAGLE (solid curves) and ILLUSTRIS (dashed curves) galaxy formation models. Blue colours correspond to active galaxies and red curves to passive galaxies. Observational data from VDW14 and Shen et al. (2003) are shown as squares, as in Fig. 1.

of active and passive galaxies in all redshift bins shown. Interestingly, the overlap in galaxy sizes of active and passive populations at $M_* < 10^{9.5}$ and $M_* > 10^{10.5}$ $M_\odot$ is seen in both simulations (as discussed in Section 3.1). While the trends are similar for both models, there is a normalization offset in the sizes. For $M_* < 10^{10}$ $M_\odot$, the ILLUSTRIS galaxies are typically a factor of 2 (0.3 dex) larger than EAGLE galaxies and those observed.

It is very hard to pinpoint the origin of the sizes differences between simulation suites because the approaches to star formation and feedback are very different. In our simulations, galaxy sizes tend to be too small if the stars form at high densities. This usually corresponds to stars forming early in the history of the Universe. Injecting greater feedback energy in dense regions helps to overcome numerical cooing issues and hence delay the formation of stars. The simulations which form larger galaxy discs also have a volume-average SFR density which evolves in good agreement with observational data. Comparing the SFR densities of the ILLUSTRIS suggests that this may well be the issue. The ILLUSTRIS simulation shows a relatively modest decline in the SFR density of the Universe towards low redshift (figs 8 and 9 of Vogelsberger 2014) in comparison to observational data (and EAGLE). These differences are most likely due to the implementation of feedback in ILLUSTRIS, in which particles are ejected depending on dark matter halo properties, and not depending on local gas properties. An in-depth investigation of the winds generated in the EAGLE simulations will be presented in Crain et al. (in preparation).

APPENDIX B: RESOLUTION TESTS

In Fig. B1, strong and weak convergence tests for the evolution of the galaxy size–mass relation are shown. Three simulations are presented: Ref-L100N1504, which was used in the main sections of this paper, Ref-L025N0752, using the same subgrid physics parameters as Ref-L100N1504 but run in a 25-cMpc box with eight times better mass resolution, and Recal-L025N0752, also in a 25-cMpc box with eight times the mass resolution but with recalibrated stellar feedback and AGN parameters to better reproduce the local stellar mass function. The details of the recalibration of the high-resolution run can be found in Schaye et al. (2015).

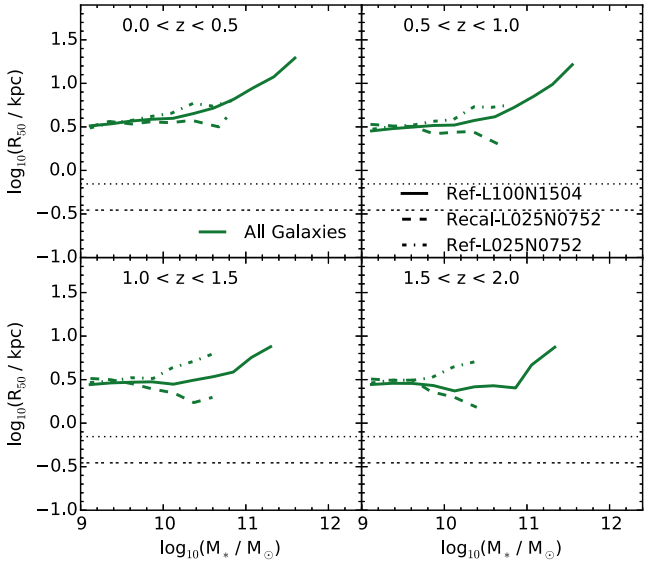

Figure B1. Comparison of sizes for galaxies from Ref-L100N1504, Ref-L025N0752 and Recal-L025N0752 over the range $0 < z < 2$ using the redshift bins in Fig. 1. The solid, dashed and dot–dashed curves correspond to the median size–mass relations of Ref-L100N1504, Recal-L025N0752 and Ref-L025N0752, respectively. The horizontal dotted and double-dotted lines indicate the gravitational force softening of the intermediate- and high-resolution EAGLE simulations, respectively. For the lowest redshift bin, a good convergence is seen between the models, and on increasing to higher redshifts, a good convergence is maintained for $M_* < 10^{10}$ $M_\odot$, but above this mass, the sizes diverge.

Comparing Ref-L100N1504 with Ref-L025N0752 tests the strong convergence of the simulation (this is the typical convergence test carried out on hydrodynamical simulations), whereas comparing with Recal-L025N0752 tests the weak convergence, a concept introduced by Schaye et al. (2015) to account for the necessity of using weakly constrained subgrid physics prescriptions. Note that more massive galaxies form in the $(100\ \mathrm{cMpc})^3$ simulation than in the $(25\ \mathrm{cMpc})^3$ simulations due to the larger box size.

In the lowest redshift bin, $0 < z < 0.5$, a reasonable agreement is seen between all simulations, although the recalibrated model, Recal-L025N0752, exhibits a downturn at $M_* \gg 10^{10}$ $M_\odot$. At $z > 1$, the size–mass relations at $M_* > 10^{10}$ $M_\odot$ of the 25 cMpc simulations diverge, with the Ref-L100N1504 simulation falling in between.

In the most massive galaxies in Recal-L025N0752, the weaker density dependence of the subgrid model for feedback from star formation, which was introduced to better reproduce the galaxy stellar mass function, allows more compact galaxies to form at high redshift relative to Ref-L100N1504. Meanwhile, in the Ref-L025N0752 simulation, massive galaxies are larger because the feedback is more efficient in high-density regions.

APPENDIX C: VARIATIONS IN GALAXY SIZE DEFINITION

We look at the variations in galaxy sizes due to the 3D spherical aperture within which the total galaxy mass is measured and the effects of projection. In Fig. C1, the variations of the median galaxy size–mass relations recovered by applying different size definitions are compared at $z = 0$, 1 and 2. The half-mass radius computed based on the total stellar mass and the mass within 3D 100- and 30-pkpc apertures yields similar galaxy sizes for stellar masses below $10^{10.5}$ $M_\odot$ (as is the case for the mass, see Schaye et al. 2015), but larger apertures result in larger sizes above this mass. In this paper, the size is defined as the half-mass radius computed based on the mass within 100-pkpc apertures. This aperture very closely replicates the half-mass radius determined by including all particles associated with a subhalo for galaxies with $M_* < 10^{11}$ $M_\odot$. However, it excludes stars far out in the most massive haloes in the simulation, which would be difficult to observe (and are labelled intracluster light).

As well as comparing the effect of different apertures, we compute projected radii and the half-mass radius based on Sérsic fits to the mass profile. These variations result in systematic offsets in the size–mass relation relative to the 3D half-mass radius measurement. Due to the systematic nature of these offsets, we present only the 3D half-mass radius measurement throughout, as variations in the definition do not impact the trends in galaxy sizes from the simulations. We note, however, that the definition of galaxies may result in a systematic decrease of up to 0.2 dex. A similar systematic offset

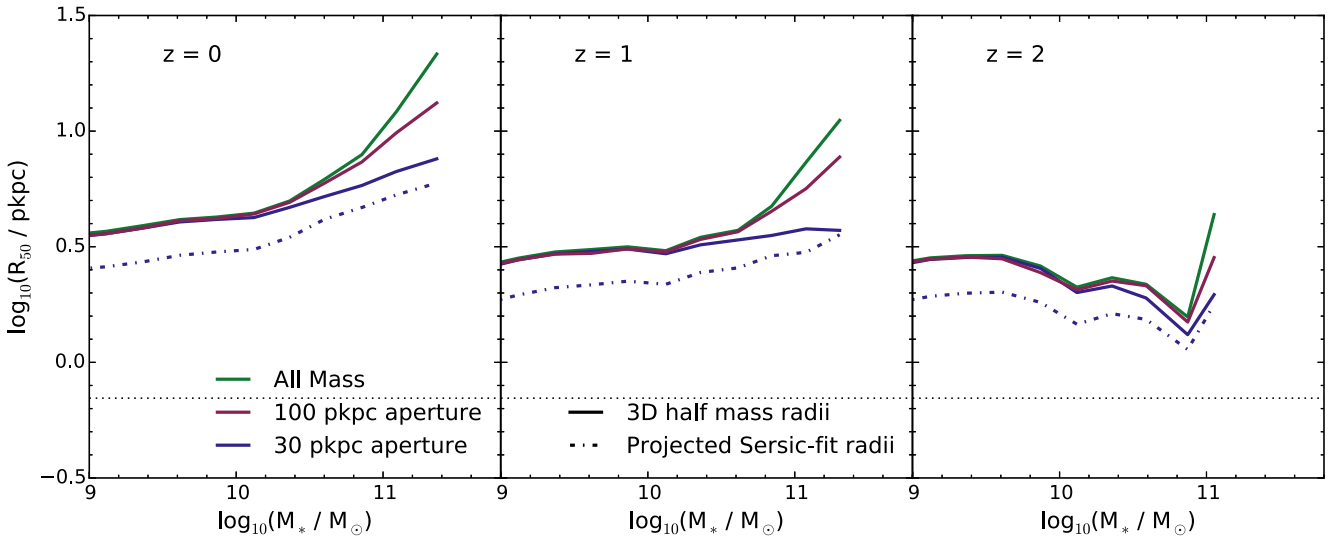

Figure C1. The median size–mass relation for galaxy sizes computed within different apertures and applying different measurement techniques at $z = 0$, 1 and 2. Solid curves show the 3D half-mass radius and dot–dashed curves show the projected half-mass radius based on a Sérsic fit to the mass profile. Green curves show the radius based on all star particles bound to the subhalo, whereas red and blue curves consider only stars within 3D 100- and 30-pkpc apertures, respectively. The solid red curves correspond to the sizes used in this work, whereas the blue dot–dashed curves indicate the sizes used by Schaye et al. (2015). The horizontal dotted line shows the gravitational force softening length in the simulation. The aperture measurements affect the galaxy sizes at stellar masses $>10^{10.5}$ $M_\odot$, with the galaxy size increasing with increasing aperture. The different size measurement techniques produce similar trends with stellar mass, but there is a small systematic offset in size. Note that we define the size as the 3D half-mass radius in a 100-pkpc aperture.

has been found when computing observed radii using circularized and non-circularized methods (Dutton et al. 2011).

APPENDIX D: DEFINITION OF PASSIVE GALAXIES

In this appendix, we discuss the impact of the definition of active and passive galaxies on the resulting difference in sizes reported between these two galaxy types (Fig. 1). As discussed in Section 2.4, the active/passive definition is based on the SSFR of a galaxy. In observations, however, where SFRs must be inferred, the definition of active and passive galaxies often depends on the observed colours of galaxies (e.g. VDW14). To determine whether any significant difference arises by applying a colour cut, as opposed to an SSFR cut, at $z = 0$, 1 and 2, we produce *UVJ* colours for all simulated galaxies with $M_* > 10^9$ $M_\odot$ and compare the median size–mass relations.

Galaxy colours from the simulation are produced by using the stellar population synthesis models of Bruzual & Charlot (2003) and applying the dust model of Charlot & Fall (2000). A full description of the method can be found in Trayford et al. (2015). We apply two colour cuts to the *UVJ* plane, that of VDW14 and that of Muzzin et al. (2013). We include the colour cut of Muzzin et al. because at low redshift, where the VDW14 sample is small (as commented on in Section 3.1), the VDW14 cut applied intersects the active or blue galaxy locus, resulting in an inappropriate division into active and passive galaxies.[6]

In Fig. D1, the median size–mass relations for simulated galaxies at $z = 0$, 1 and 2 are shown for all three definitions of active and passive galaxies: SSFR, *UVJ* applying the cut of VDW14 and *UVJ* with the cut of Muzzin et al. The median sizes of active galaxies are similar at all redshifts shown, irrespective of the details of the classification. For passive galaxies, there is always a clear offset from the sizes of active galaxies, but the median sizes of the passive galaxies show some variation between the cuts. This is due to the different numbers of galaxies selected depending on the specifics of the cut. Note that at $z = 2$ the sample of passive galaxies selected from the simulation is small, as, for all cuts, the galaxies are predominantly active. This causes some noise in the size–mass relation at this redshift.

Note that the impact of the definition of passive galaxies on the passive fraction is explored in more detail in Trayford et al. (2016).

In summary, how galaxies are classified results in a negligible difference in the sizes of active galaxies, whereas the same is true for low-redshift passive galaxies. For all cuts, the active/passive galaxy size offset is maintained.

[6] Note that Trayford et al. (2015) showed that at $z = 0.1$, the galaxy colours produced by EAGLE are in good agreement with observations; so for a larger observational sample, a similar issue may arise when applying the *UVJ* cut of VDW14.

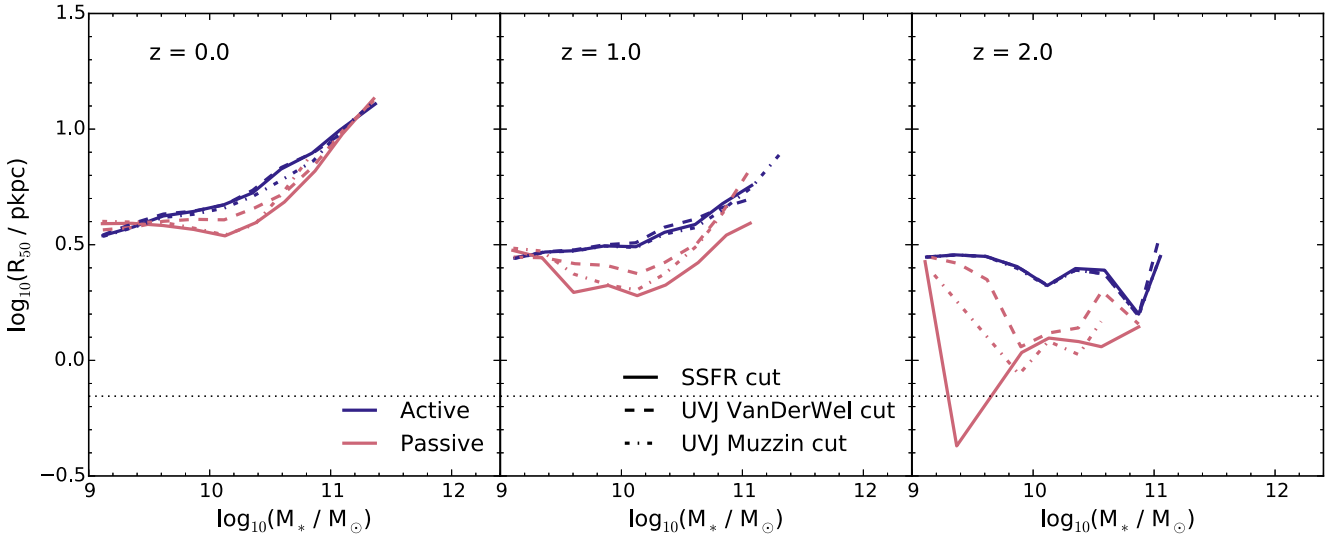

Figure D1. The median size–mass relation for different definitions of galaxy size at redshifts 0, 1 and 2 using three separations of active and passive galaxies. The dotted line corresponds to the gravitational softening of the simulation. At redshift 0, there is a good correspondence between the different definitions. At redshifts 1 and 2, differences appear for the passive galaxies due to the different numbers of galaxies identified by each method; however, the offset in size between active and passive galaxies is evident for all three definitions. Note that the noise in the $z = 2$ passive galaxy sample is due to the small number of passive galaxies in the simulation at such a high redshift.

This paper has been typeset from a TEX/LATEX file prepared by the author.